12-2021

Deep Learning-Guided Prediction of Material's Microstructures and Applications to Advanced Manufacturing

Jianan Tang
jianant@g.clemson.edu

Clemson University

TigerPrints

All Dissertations   Dissertations

12-2021

Deep Learning-Guided Prediction of Material's Microstructures and Applications to Advanced Manufacturing

Jianan Tang

DEEP LEARNING-GUIDED PREDICTION OF MATERIAL'S MICROSTRUCTURES AND APPLICATIONS TO ADVANCED MANUFACTURING

A Dissertation
Presented to
the Graduate School of
Clemson University

In Partial Fulfillment
of the Requirements for the Degree
Doctor of Philosophy
Electrical and Computer Engineering

by
Jianan Tang
December 2021

Accepted by:
Dr. Hai Xiao, Committee Chair
Dr. Fei Peng
Dr. Joshua Tong
Dr. Yongkai Wu
Dr. Adam Hoover

ABSTRACT

Material microstructure prediction based on processing conditions is very useful in advanced manufacturing. Trial-and-error experiments are very time-consuming to exhaust numerous combinations of processing parameters and characterize the resulting microstructures. To accelerate process development and optimization, researchers have explored microstructure prediction methods, including physical-based modeling and feature-based machine learning. Nevertheless, they both have limitations. Physical-based modeling consumes too much computational power. And in feature-based machine learning, low-dimensional microstructural features are manually extracted to represent high-dimensional microstructures, which leads to information loss.

In this dissertation, a deep learning-guided microstructure prediction framework is established. It uses a conditional generative adversarial network (CGAN) to regress microstructures against numerical processing parameters. After training, the algorithm grasps the mapping between microstructures and processing parameters and can infer the microstructure according to an unseen processing parameter value. This CGAN-enabled approach consumes low computational power for prediction and does not require manual feature extraction.

A regression-based conditional Wasserstein generative adversarial network (RCWGAN) is developed, and its microstructure prediction capability is demonstrated on a synthetic micrograph dataset. Several important hyperparameters, including loss function, model depth, number of training epochs, and size of the training set, are

systematically studied and optimized. After optimization, prediction accuracy in various microstructural features is over 92%.

Then the RCWGAN is validated on a scanning electron microscopy (SEM) micrograph dataset obtained from laser-sintered alumina. Data augmentation is applied to ensure an adequate number of training samples. Different regularization technologies are studied. It is found that gradient penalty can preserve the most details in the generated microstructure. After training, the RCWGAN is able to predict the microstructure as a function of laser power.

In-situ microstructure monitoring using the RCWGAN is proposed and demonstrated. Obtaining microstructure information during fabrication could enable accurate microstructure control. It opens the possibility of fabricating a new kind of materials with novel functionalities. The RCWGAN is integrated into a laser sintering system equipped with a camera to demonstrate this novel application. Surface-emission brightness is captured by the camera during the laser sintering process and fed to the RCWGAN for online microstructure prediction. After training, the RCWGAN learns the mapping between surface-emission brightness and microstructures and can make prediction in seconds. The prediction accuracy is over 95% in terms of average grain size.

DEDICATION

This dissertation is dedicated to my family and friends,

for their endless love and support.

ACKNOWLEDGMENTS

TABLE OF CONTENTS

LIST OF TABLES

LIST OF FIGURES

List of Figures (Continued)

CHAPTER ONE

INTRODUCTION

In advanced manufacturing, material microstructure prediction based on processing conditions could be very useful. It is because to the material's properties are largely determined by its microstructure, and the microstructure is greatly affected by the processing conditions [1]. These relationships are also known as process-microstructure-property linkages [2,3,4]. Conventionally, material development demands the process-microstructure-property linkages to be established through trial-and-error experiments. Numerous combinations of processing conditions need to be exhausted, and the resulted microstructures have to be characterized offline (e.g., SEM). Both of them are time and resource-consuming. With microstructure prediction capability, microstructure information can be obtained right after the sample is fabricated, which saves a huge amount of time in microstructure characterization and accelerates the material development cycle. Furthermore, when this microstructure prediction capability is combined with in-situ monitoring techniques, it is possible to acquire microstructure information during the fabrication process. It leads to high-precision microstructure control and opens the possibility of fabricating novel devices enabled by specially designed microstructure profiles.

1.1 Process-microstructure-property relationship

Knowledge about process-microstructure relationships is essential to guide the fabrication processes. It basically concerns what the microstructure looks like when the

material undergoes a certain process. It is important because the material's properties are largely determined by the microstructure, which is also known as the microstructure-property relationship [5]. For example, in metallurgy, the strength of the material is inversely proportional to the grain size [6]. In proton conduct ceramics, the electrical conductivity is proportional to the grain size [7]. Wen Lien et al. studied the microstructure-property relationship in a lithium disilicate glass-ceramic and concluded that with more lithium disilicate formed, higher elastic modulus and hardness could be obtained [8]. In summary, controlling the microstructure is essential to obtain the material with the desired properties.

Trial-and-error experiments have been the common practice to guide fabrication process optimization. In trial-and-error experiments, multiple samples are fabricated using various processing parameters. Then the microstructures of the samples are characterized through scanning electron microscopy (SEM). The obtained microstructure data are analyzed to find the correlation between microstructural features and the processing parameters. When a multi-pass rolling process was used to fabricate metal sheets, experimental results suggested that temperature significantly affected the grain size and elongation [9]. Spinelli et. al. found that in strip casting, columnar dendritic microstructures formed on the sample surface [10]. Experimental results suggested that when the cooling rate was larger, the dendritic spacing was smaller. Wang et al. investigated the sintering temperature effect on the microstructure of titanium diboride ceramics sintered in a hot-pressing furnace [11]. They found that when sintering time was held at 60 min, the grain size and the relative density increased when the sintering

temperature increased from 1773 K to 2173 K. Similar relationship was observed when Mahmoud et al. sintered titania gel in an electrical furnace [12]. The sintered ceramic was nanoporous titania, whose pore size decreased when the sintering temperature increased.

The trial-and-error approach is also applied to laser-based material processing methods, such as laser welding [13], laser sintering [14], laser melting [15], and laser drilling [16]. Microstructures formed from laser-based processing methods tend to be different from conventional methods because of localized effects and high heating rates [17]. Empirical knowledge accumulated from the conventional fabrication methods cannot be directly applied. New experimental data are needed to identify the process-microstructure relationships in laser-based processing methods. Ghaini et al. investigated the microstructure formed under pulsed Nd:YAG laser welding [18]. Within the explored range, they found that with lower heat input, which means lower laser power or higher travel speed, fine columnar dendrites were the dominant microstructure. Increasing the heat input resulted in coarser structures. Thijs et al. studied the effect of processing parameters on the microstructure formed during selective laser melting of Ti-6Al-4V [19]. Elongated grains were observed whose direction depended on the laser scanning strategy. Mu et al. demonstrated laser sintering of $BaCe_{0.7}Zr_{0.1}Y_{0.1}Yb_{0.1}O_{3-\delta}$ (BCZYYb), a proton conductive ceramic material [20]. The resulted microstructure could be engineered by varying laser processing parameters.

In conclusion, the current practice of material development to establish process-microstructure linkages consists of three steps. The first step is sample fabrication. Then SEM micrographs are taken on the samples to characterize the microstructures. In the

3

end, the obtained SEM micrographs are analyzed by experts. Microstructure characterization and analysis can take a large amount of time. While laser-based advanced manufacturing technologies have accelerated sample fabrication from hours to minutes, microstructure characterization and analysis have to be expedited as well, which could be solved by microstructure prediction.

1.2 Physical-based modeling

Physical-based modeling and numerical methods that can predict microstructures are investigated to accelerate material research. One of the most successful tools is the phase-field models [21]. The phase-field models have been applied to predict microstructure evolution for various material processes [22], such as grain growth, crack propagation, and solid-state phase transformation. Wang et al. developed a phase-field model for the solid-state sintering process [23]. The model successfully predicted the microstructure evolution, such as neck formation and grain boundary migration. Echebarria et al. demonstrated that a phase-field model could make quantitative predictions for the solidification process of a binary alloy [24]. Takaki employed a phase-field model to simulate large-scale dendrite growth that was often observed during the casting of metal materials [25].

Phase-field models also achieved great success in laser-based processing methods. Li et al. used a phase-field model to simulate the solid-liquid phase transition along with the thermocapillary effect during laser melting of a single metallic powder [26]. Zhang et al. proposed a phase-field model to predict microstructure behaviors during solid-state

selective laser sintering of metallic materials [27]. Microstructure features such as neck size between adjacent particles were accurately predicted. Yang et al. introduced non-isothermal assumption into a three-dimensional phase-field model to simulate microstructure evolution during selective laser sintering [28]. The predicted microstructure agreed well with experimentally obtained SEM micrographs. They then used the model to investigate the effect of laser power and scanning speed on the porosity.

While the phase-field models have gradually become the standard approach to simulate microstructure evolution and analyze process-microstructure relationships theoretically, there are some drawbacks that prevent them from wide adoption. First, developing phase-field models is not trivial. Different assumptions, constraints, and configurations need to be carefully examined and chosen to produce accurate results. For example, in Yang's work, they demonstrated that the non-isothermal assumption was necessary to address the coupling of heat transfer and microstructure evolution [28]. Second, phase-field models require a large amount of computational power. As a numerical simulation method, phase-field models demand thousands of spatial grid points and hundreds of time sampling points to make accurate predictions. The amount of computational power makes it impossible for users without access to supercomputers or high-performance computing clusters. In Yang's work, microstructure evolution from 0 μs to 5000 μs in a 100 μm × 500 μm ×250 μm cube under the laser spot was simulated. The simulations were performed with 150 processors, and each simulation consumes about 10000 CPU cores×hours. Miyoshi et al. conducted an ultra-large-scale phase-field

simulation of ideal grain growth [29]. The most accurate result was obtained by assigning 2560^3 grid points to the model. The computation has to be conducted on the supercomputer TSUBAME2.5.

1.3 Machine learning approach

Due to the abundance of data accumulated in the past decades and the rapid increase of computational power, machine learning has revolutionized many aspects of our lives. From recommending system [30] to fraud detection [31], from speech recognition [32] to chatting robots [33], from optical character recognition [34] to objective detection and localization [35], machine learning algorithms have achieved unprecedented success. Apart from the computer science community, machine learning algorithms have also attracted many researchers in other areas for relatively low computational cost and high accuracy [36, 37, 38].

In the material science community, scientists and engineers are thrilled with the possibility that machine learning tools can accelerate material discovery, process design, microstructure characterization, and property optimization [39]. A significant number of papers propose and demonstrate using machine learning algorithms to explore microstructure-property relationships. Convolutional neural networks (CNNs) [40] are one of the most popular machine learning algorithms in this application. Yang et al. combined principal component analysis (PCA) and CNN to predict the stress-strain curve of a composite material based on its microstructure [41]. The mean absolute error of prediction was below 10%. Cecen et al. employed a three-dimensional CNN to model the

linkage between three-dimensional microstructures and their elastic properties [42]. The mean absolute error of prediction was 11.3%. Herriott et al. did similar work utilizing CNN to predict mechanical properties of additively manufactured metals based on microstructure features [43].

Using machine learning approaches to predict microstructure based on processing parameters is attractive. Hashemi et al. developed a machine learning framework to predict microstructure evolution [44]. They first extracted low-dimensional microstructural features from the microstructures based on two-point spatial correlations. Then they trained a Gaussian process autoregression model to predict the evolution of these low dimensional features. Similar work has been done by Brough et al. in studying the microstructure evolution in polyethylene films [45]. Brough then formalized this approach and demonstrated that it is three times faster than numerical simulations [46].

The machine learning approach reviewed above is feature-based. It faces two challenges. First, how to extract low-dimensional features from real microstructures is still an open question. There is no well-established method to reliably recognize, quantify, and extract a wide range of microstructure features from real micrographs. Second, predicting microstructural features rather than microstructure itself inevitably leads to information loss. It is because the microstructure, which is often represented as SEM micrographs, contains numerous features. Representing a microstructure with a limited number of features is omitting other features that could hold important information.

1.4 Generative adversarial network

Generative adversarial networks (GANs) are one of the most popular deep learning algorithms proposed by Ian Goodfellow in 2014 [47]. GANs are able to generate highly authentic images with respect to the training data. This capability has invoked many amazing applications. Karras et al. developed a progressive growing GAN (ProGAN) to synthesize high-quality and high-resolution human face images [48]. Soon they take a step forward to incorporate additional information, known as style, to generate human face images with adjustable features, such as skin color, facial expression, hairstyle [49]. Hamada et al. utilized an augmented ProGAN to synthesize anime clips with a character changing its pose [50]. Alsaiari et al. developed a GAN that was able to denoise images [51].

Using GANs to synthesize microstructures is attractive. Compared with the experimental approach and physical-based modeling, GANs can produce the same quality microstructures with much larger quantities in a short time [52]. Gayon-Lombardo et al. employed a deep convolutional GAN (DC-GAN) to generate three-phase electrode microstructures based on real X-ray computed tomography images [53]. The generated micrographs shared the same statistical features, such as phase volume fraction, with the real data. They claimed that this approach can generate an arbitrary large volume of authentic (statistically similar to real data) microstructures and thus explore microstructure space efficiently. Li et al. proposed a GAN-based framework that can accelerate microstructure design [54]. They used a GAN to stochastically generate realistic microstructures and computed the corresponding properties via physical

simulations. The computed properties were fed to an optimization model, which guided

the optimization of generated microstructure. By doing so, the optical absorption of the

resulted microstructure was improved by 15%. Chun et al. introduced a morphology

parameter to control GAN-generated microstructures [55]. This approach enabled more

controllability on the generated microstructure and could synthesize unseen

microstructures.

Conditional GAN (CGAN) is a variant of GANs that allows users to incorporate

additional information (condition) into image synthesize and control certain features by

doing so [56, 57]. It is possible to look into process-microstructure relationships using

CGANs with processing parameters as the conditions. Some preliminary research has

been published in this direction. Iyer et al. generated authentic metal microstructures

formed under different cooling methods [58]. Banko et al. used the concentration of Al

and deposition temperature as the conditions to model the relationship between the

processing parameters and the thin film microstructure [59].

1.5 Laser sintering

Laser sintering [14, 60, 61] is one of the most rapidly growing advanced

manufacturing technologies because of two reasons. First, in laser sintering process,

dense products are fabricated in a short time compared with conventional sintering

methods, such as furnace sintering. Second, the laser sintering process offers unparallel

flexibility in terms of materials, microstructures, and geometries. Material-wise, laser

sintering can process almost many kinds of materials, such as polymers, metals, ceramics,

and glass. By varying processing parameters at different locations, heterogenous

microstructures can be obtained. Products of arbitrary geometry can be produced by a layer-wise fabrication procedure. By combining those two advantages together, laser sintering technology can rapidly fabricate novel products with complex 3D geometry, heterogeneous microstructures, and unique properties.

In the laser sintering process, raw material powders absorb the laser energy and are heated up rapidly. Under the elevated temperature, the raw material powders experience multiple physical or even chemical processes, such as sintering, melting, vaporization, thermomechanical shock, and plasma formation [62, 63, 64]. When the laser spot moves away, the local temperature drops quickly. This rapid heating and cooling result in unique microstructures that cannot be obtained by conventional fabrication methods [17]. While it opens the possibility for new materials with novel properties and functionalities, investigations into the process-microstructure-property relationships are difficult.

There are three reasons why investigating the process-microstructure relationship in the laser sintering process with a CGAN-based approach is particularly attractive. First, after the CGAN is trained, it can make predictions very fast. Second, a CGAN can directly predict microstructures rather than microstructural features. Third, high-throughput experiments can be designed and conducted with the laser sintering process to produce enough data to train machine learning algorithms [65].

1.6 In-situ monitoring in laser-based advanced manufacturing processes

The phrase "Fourth Industrial Revolution", or "Industry 4.0" was first introduced by the German government in 2015 and was the focus of the World Economic Forum 2016 [66, 67]. The core concept of Industry 4.0 is the "smart manufacturing", which emphasizes sensing, monitoring, automation, and data communication between machines [68, 69]. Thus, in-situ monitoring during the manufacturing process plays an important role in "smart manufacturing".

Extensive efforts have been spent on developing in-situ monitoring and sensing methods for laser-based advanced manufacturing systems, especially powder bed fusion systems [70]. In powder bed fusion systems, a high-power laser melts the powders together to form a melting pool, which then solidifies to the consolidated structure. The stability, shape, and temperature of the melting pool are recognized to be important features that determine the quality of the final product. Clijsters et al. used a camera and a photodiode to measure the thermal emission intensity and geometry of the melting pool [71]. By doing so, they identified the overheating points where the melting pool area was above a threshold. The pores formed due to the disturbance of the melting pool were then found. Zhang et al. adopted a computer vision approach to track the melting pool [72]. Using the Kalman filter, they successfully identified the melting pool when there were many spatters with similar shapes and brightness.

Despite the huge progress that has been achieved in in-situ monitoring methods, no microstructure information has been extracted during laser processes. All microstructure characterizations have to be conducted offline. In-situ monitoring of

material's microstructure is extremely challenging but highly desirable. Once in-situ microstructure monitoring is realized, the properties of the material at different positions can be precisely controlled. It opens the possibility of manufacturing many novel products that cannot be fabricated using traditional methods.

1.7 Motivation and objectives

1.7.1 Motivation
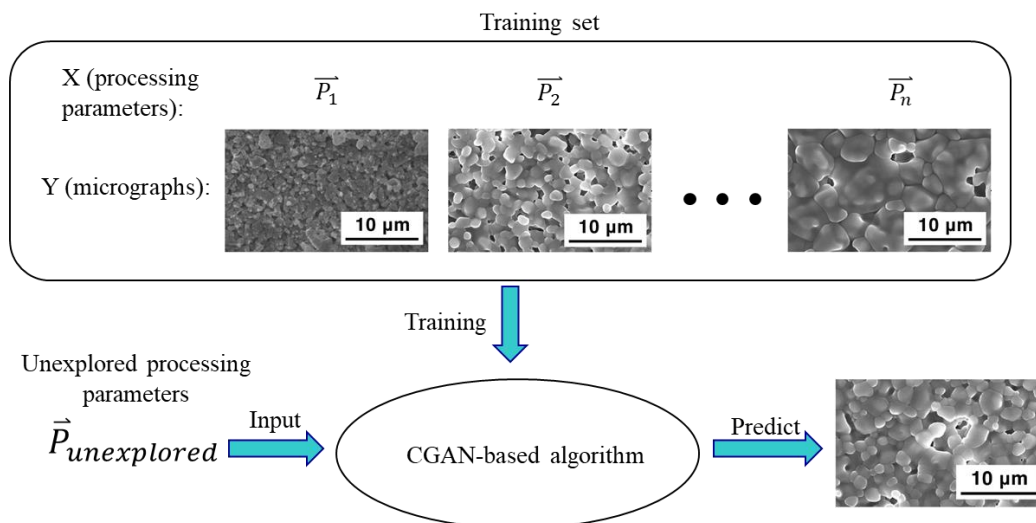
Figure 1.1 Approach to train a CGAN-based algorithm and predict the microstructure according to unexplored processing parameters.

A fast microstructure prediction method is needed to accelerate the material development cycle because trial-and-error experiments consume too much time and resources. Physical-based modeling can predict microstructures. But it takes too much computational power to run one simulation. Machine learning approaches have been proposed and investigated by researchers. They are computationally cheap, but feature extraction is often required. Feature extraction can lead to information loss. In the

meantime, there has been no well-established method to extract features from SEM micrographs.

To overcome these limitations, I propose to use a conditional generative adversarial network to regress microstructures against processing parameters. After the CGAN is trained, it can predict the microstructure given the processing parameters that have not been experimentally explored, as shown in Figure 1.1. If the prediction is accurate and fast, the material development cycle will be accelerated.

1.7.2 Objectives

The main objective is to establish a methodology of using a CGAN to accurately predict microstructures based on processing parameters and evaluate the prediction accuracy. The following specific objectives are met with this research:

1) Develop a methodology to train, validate, and optimize a CGAN.

2) Validate the DL-based microstructure prediction by using laser power as an example processing parameter.

3) Propose and demonstrate an in-situ monitoring microstructure method using the CGAN.

1.8 Organization of the dissertation

This dissertation is organized into six chapters with their contents briefly described below:

Chapter 1 gives a general introduction to research about microstructure prediction. A brief review of the existing methods including trial-and-error experiments, physics-based modeling, and feature-based machine learning is provided. The limitations

of each method are summarized. A new approach based on deep learning is proposed. Some related work is reviewed.

Chapter 2 describes the procedure to develop a customized CGAN that aims to predict microstructures based on processing parameters. A synthetic microstructure dataset is established, where the grain size distribution changes with a processing parameter. The prediction accuracy of the algorithm is quantitatively evaluated in terms of how accurate it can predict the mean aspect ratio and grain size distribution. The effect of various hyperparameters on performance is studied. We name the optimized algorithm Regression-based conditional Wasserstein Generative Adversarial Network (RCWGAN).

Chapter 3 is a case study where the RCWGAN is applied to predict microstructures of laser-sintered alumina based on laser power. Experimental procedures for obtaining laser-sintered alumina's microstructures are described. The predicted microstructure is compared with the real microstructure to prove that the prediction is accurate.

Chapter 4 demonstrates how to monitor the microstructure during the laser sintering process based on in-situ captured surface-emission brightness using the RCWGAN. The laser-based manufacturing system described in chapter 3 is modified to add in-situ monitoring capability. The correlation between the surface-emission brightness and the microstructure is presented. After the RCWGAN is trained, its prediction accuracy and speed is tested.

Chapter 5 summarizes the work in this dissertation and comments on the future of the research.

1.9 Innovation and contributions

Major scientific and technical contributions of this dissertation include the following:

1) Proposed a new concept of using deep learning to predict material microstructures during advanced manufacturing.

2) Reviewed different methods for microstructure prediction and analyzed their pros and cons.

3) Proposed to use conditional GAN to regress microstructures against processing parameters and make predictions.

4) Established a methodology to train, validate, and optimize the RCWGAN quantitatively.

5) Systematically studied important hyperparameters, including model depth, training epochs, and training set size.

6) Validated the DL-based microstructure prediction by using laser power as an example processing parameter. The prediction is accurate under qualitative examination.

7) Studied and compared two regularization techniques: weight clipping and gradient penalty.

8) Proposed an in-situ monitoring microstructure method using the RCWGAN.

9) Proved the RCWGAN is capable of accurate and fast microstructure prediction based on surface-emission brightness during laser sintering.

CHAPTER TWO

PREDICTING MICROSTRUCTURE WITH CONDITIONAL GENERATIVE ADVERSARIAL NETWORKS

In this chapter, a CGAN that can accurately predict microstructures is implemented. The CGAN is trained on a synthetic micrograph dataset whose grain size distribution is controlled by a hypothetical processing parameter λ. Many hyperparameters, such as loss function and model depth, are studied to optimize the algorithm's performance. The prediction accuracy is quantitatively evaluated by comparing the grain size distribution of predicted microstructures and the real ones.

2.1 Synthesized micrograph dataset

The CGAN is first demonstrated on a synthetic micrograph dataset for two reasons. First, the microstructure features, like grain size distribution, are relatively easy to measure on synthetic micrographs, while the grain boundaries in real micrographs are much harder to identify. Second, establishing a synthetic micrograph dataset is much easier than a real microstructure dataset. A synthetic micrograph dataset can be produced by a computer program in ten minutes, while a real microstructure dataset usually requires tens of hours of experiments.

The synthetic micrograph dataset consists of seven subsets, each of which is labeled by a distinct λ value from 1 to 7. In one micrograph subset, there are 5,000 synthetic micrographs. One synthetic micrograph has about 20 randomly distributed black dots representing grains. The grain size distribution follows a lognormal distribution whose mean linearly increases with λ. Some examples are shown in Figure

2.2. Six micrograph subsets labeled by 1,2,3,5,6, and 7 are used for training, while the one labeled by 4 is used to test the prediction accuracy.

2.2 Conditional GAN
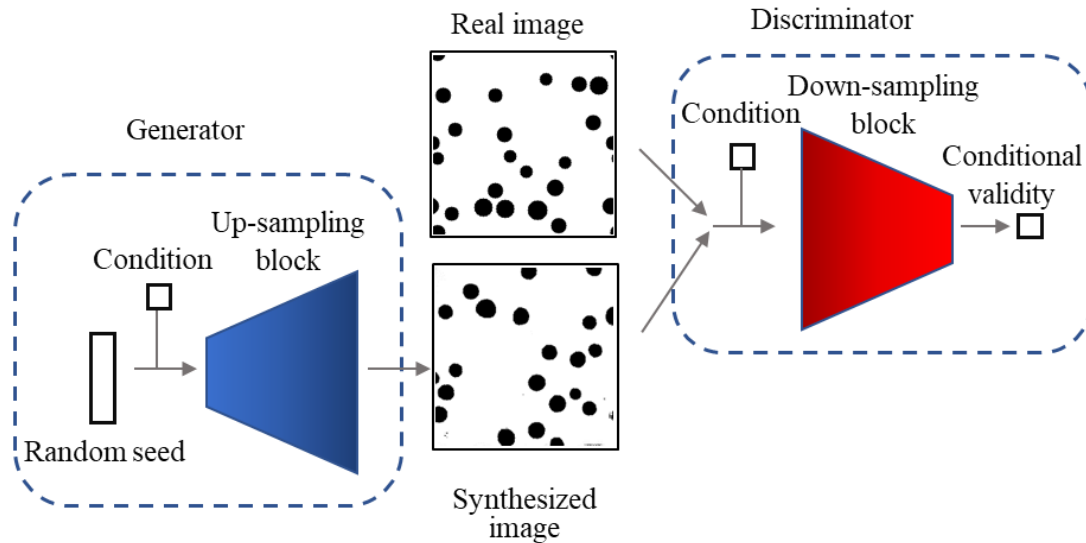
Figure 2.1. The structure of a CGAN.

In Figure 2.1, the structure of a CGAN is shown. The CGAN consists of a generator and a discriminator. The generator takes a random seed and a condition to generate an image. In this case, the condition is the processing parameter λ. The discriminator takes an image, generated or real, and the condition to give a conditional validity score. The validity score represents how confident the discriminator is about the input image to be real.

During training, the generator gets better at generating plausible images according to the processing parameter, and the discriminator improves at distinguishing the

generated images from the real images. After the algorithm is properly trained, the generator should be able to generate images that look just like real ones.

Figure 2.2 shows the approach to train, validate and optimize the CGAN on the synthetic micrograph dataset. First, the CGAN is trained on the dataset. Then, the CGAN predicts a microstructure based on a new processing parameter value. Then the predicted microstructure is quantitatively compared with the real one. The validation result is used to guide optimization of hyperparameters like loss function and network structure.
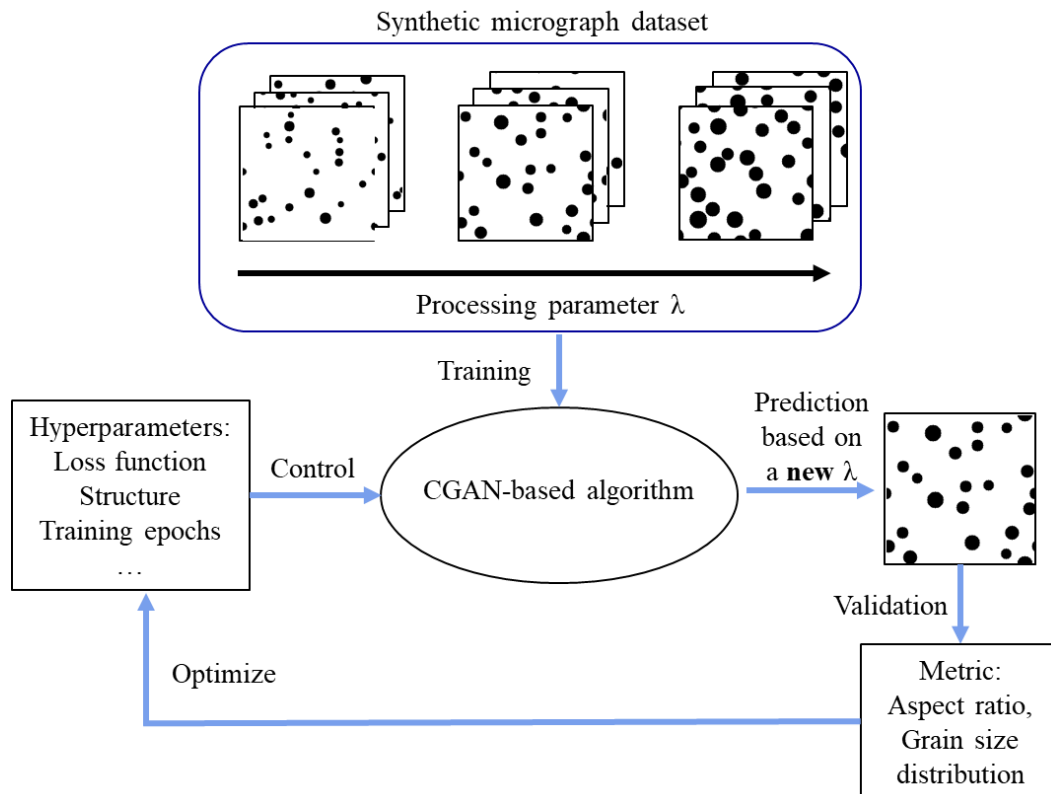
Figure 2.2. The approach to train, validate, and optimize a CGAN on a synthetic micrograph dataset.

2.3 Quantitative evaluation metrics

To quantitatively evaluate the prediction accuracy, the real micrographs and the predicted micrographs are compared in three microstructural features: aspect ratio, average grain size, and grain size standard deviation. The microstructural features of the real micrographs are measured with the region proposal algorithm in Matlab. It basically joins all neighboring pixels with the same black color to form regions. The size, major axis length, and minor axis length of a region are also measured by the algorithm. It is worth noting that some grains are cropped by the edges, which causes the measured features to differ from the designed value. To reduce the edge effect, if the distance of a grain's center to the edge is less than 15 pixels, this grain will not be counted when the microstructural features are measured. 1,000 real micrographs under λ equal to 4 are measured. The measured aspect ratio is 1.04. The average grain size is 11.00, and the grain size standard deviation is 2.10. The aspect ratio slightly differs from the real value 1 because the edge effect has been greatly reduced.

The predicted micrographs will also be measured under the protocol described above. Then the microstructural features of the predicted micrographs and the real micrographs will be compared. The prediction accuracy will be reported in relative error, which is calculated as following:

$$relative\ error = \left| \frac{predicted\ value}{real\ value} - 1 \right| \tag{1}$$

2.4 Study the hyperparameters

2.3.1 Loss function

The original GAN uses the following loss function [47]:

$$L(x, \hat{x}) = \log\left(\sigma\left(D_w(x)\right)\right) + \log\left(1 - \sigma\left(D_w(\hat{x})\right)\right) \quad (2)$$

where x represents the real micrograph, $\hat{x}$ is a generated micrograph, D_w stands for the discriminator, and σ is the sigmoid function.

This loss function measures the Jenson-Shannon divergence between the generated distribution and the real distribution. When the discriminator is trained, the weights in the discriminator are updated to make $\sigma\left(D_w(x)\right) = 1$ and $1 - \sigma\left(D_w(\hat{x})\right) = 0$, under which the loss function is maximized. When the generator is trained, the derivative is:

$$\frac{\partial L}{\partial \hat{x}} = \sigma\left(D_w(\hat{x})\right)\frac{\partial D_w(\hat{x})}{\partial \hat{x}} = 0 \times \frac{\partial D_w(\hat{x})}{\partial \hat{x}} = 0 \quad (3)$$

As a result, the generator does not get updated. This is also known as gradient vanishing.

Arjovsky et al. proposed to use the Wasserstein distance as the loss function [73] to overcome this problem. The Wasserstein distance can provide a useful gradient to update the generator and consequently stabilize the training. Many researchers have achieved good performance with Wasserstein loss function [74, 75]. The Wasserstein loss function is:

$$L(x, \hat{x}) = D_w(x) - D_w(\hat{x}) \quad (4)$$

Figure 3 shows a comparison among the real micrographs, predicted micrographs with the JS loss function, and predicted micrographs with the Wasserstein loss function. Due to the reason stated above, when using the JS loss function, the generator fails to converge. The micrographs predicted under $\lambda = 4$ are nothing like the real micrographs. On the contrary, the micrographs predicted with the Wasserstein loss function have very similar patterns to the real ones. A predicted micrograph has about 18 black dots randomly distributed. The sizes of the black dots follow a distribution much like the real ones.

Real   JS divergence   Wasserstein distance
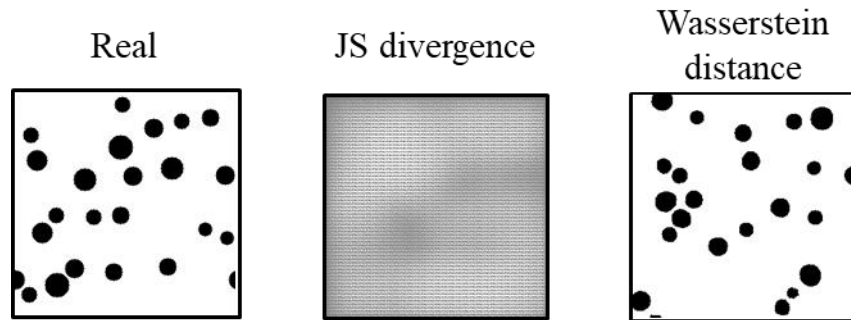
Figure 2.3. Examples of a real micrograph and predicted micrographs with different loss functions.

To quantitatively measure the prediction accuracy, 1,000 micrographs are generated using the trained generator and measured for microstructure features. The mean aspect ratio is calculated to be 1.10. The average grain size is 10.03, and the grain size standard deviation is 1.80. The relative error in the mean aspect ratio is 5.77%, which suggests the algorithm understands that most grains are round except some that are cropped by the edge. The relative error in the average grain size is 8.90%. And the relative error in grain size standard deviation is 18.92%.

2.3.2 Depth of the model

In deep learning, the depth of the model plays an important role in improving the model's performance. When Lecun proposed LeNet in 1995 [76], the network had only 5 layers. The algorithm performed well on a hand-written digit dataset and reached a 0.9% classification error. However, when the images to be processed contain more complex features and have more pixels, deeper models are needed to extract higher-level features and distinguish them. In 2012, Krizhevsky et al. proposed AlexNet that had 11 layers [77]. It won the ImageNet Large Scale Visual Recognition Challenge (ILSVRC) in 2012 with a top-5 error of 15.3%. Later on, K. Simonyan and A. Zisserman from the University of Oxford proposed the VGG-16 [78]. It had 16 layers and reduced top-5 error to 7.3%. In 2015, Szegedy et. al. from Google invented GoogleNet [79]. The GoogleNet utilized a special structure named "Inception module" to increase the depth of the network and reduce the computational cost at the same time. The GoogleNet had 22 layers but only 5 million parameters, while the VGG-16 had 138 million parameters. And the GoogleNet won the ILSVRC-2014 with a top-5 error of 6.7%.

The success of GoogleNet suggests the improvement in performance and reduction in computational cost can be achieved simultaneously. The same design guideline might be applied to the CGAN to improve the accuracy as well. At the beginning, the structure of the CGAN's generator follows the same design as the Deep Convolution GAN (DCGAN), a benchmark GAN proposed by Radford et al. in 2015. The structure of the generator is shown in Figure 2.4. "Transposed Conv5, stride 2, 128" stands for a convolutional layer with 128 5×5 kernels with the stride equal to 2.
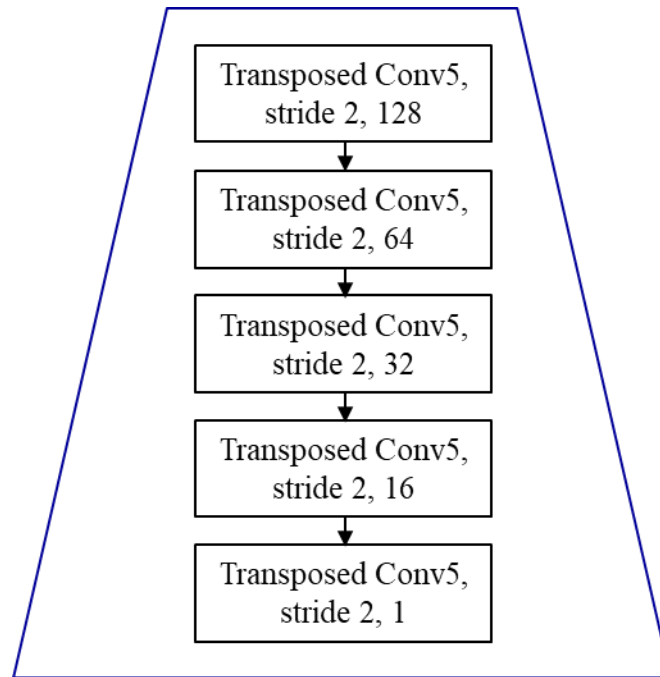
Figure 2.4. A generator structure designed follow the DCGAN.

By stacking strided transposed convolutional layers with 5×5 kernels, the generator can predict the micrographs with 8.90% relative error in average grain size. As discussed in [79], a 5×5 kernel can be factorized into two 3×3 kernels. A convolutional layer with 5×5 kernels can be replaced by two stacked convolutional layers with 3×3 kernels. Another point raised in [79] is that using convolutional layers with 1×1 kernels can reduce the number of channels of a feature map while preserving most of the information. By doing so, the depth and the nonlinearity of the model is increased while the number of parameters is reduced. Inspired by the two design guidelines described above, a stack of a convolutional layer with 1×1 kernels, two convolutional layers with

3×3 kernels, and an up-sampling layer is proposed to replace the strided transposed convolutional layer with 5×5 kernels.
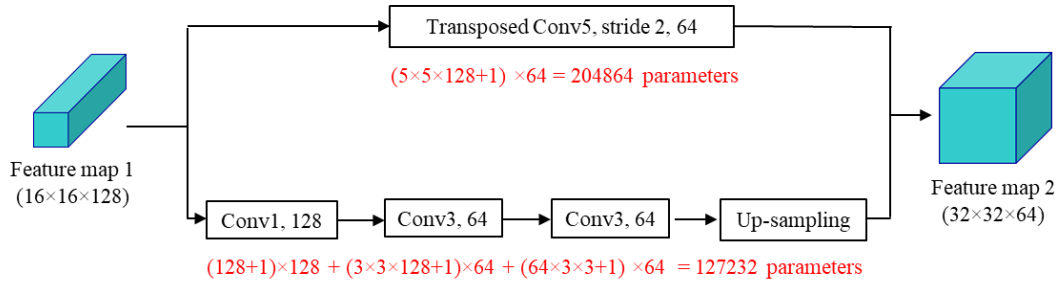
Figure 2.5. Illustration of two ways to process a feature map.

Figure 4 shows an example that replacing one strided transposed convolutional layer with a stack of convolutional layers and an up-sampling layer can reduce the number of parameters while increasing the depth of the model. In this example, a feature map of shape 16×16×128 needs to be transformed into a feature map with shape 32×32×64. One approach is passing the original feature map through a transposed convolutional layer with 64 5×5 kernels and stride 2. In this way, (5×5×128+1) ×64 = 204864 parameters are needed. Another way to do it is processing the original feature map with one convolutional layer with 128 1×1 kernels, 2 convolutional layers with 64 3×3 kernels, and an up-sampling layer subsequently. (128+1)×128 + (3×3×128+1)×64 + (64×3×3+1) ×64 = 127232 parameters are needed. By replacing the strided transposed

convolutional layer with the stack of the convolutional layers and the up-sampling layer,

the depth increases from 1 to 4 while the number of parameters decreases by 37.89%.

Conv1, 256		
Upsampling		Transposed Conv7, 16
Conv1, 128		Conv1, 8
Conv3, 64		Conv3, 4
Conv3, 64		Conv3, 4
Upsampling		Transposed Conv7, 4
Conv1, 32		Conv11, 1
Conv3, 16		
Conv3, 16		
Upsampling		
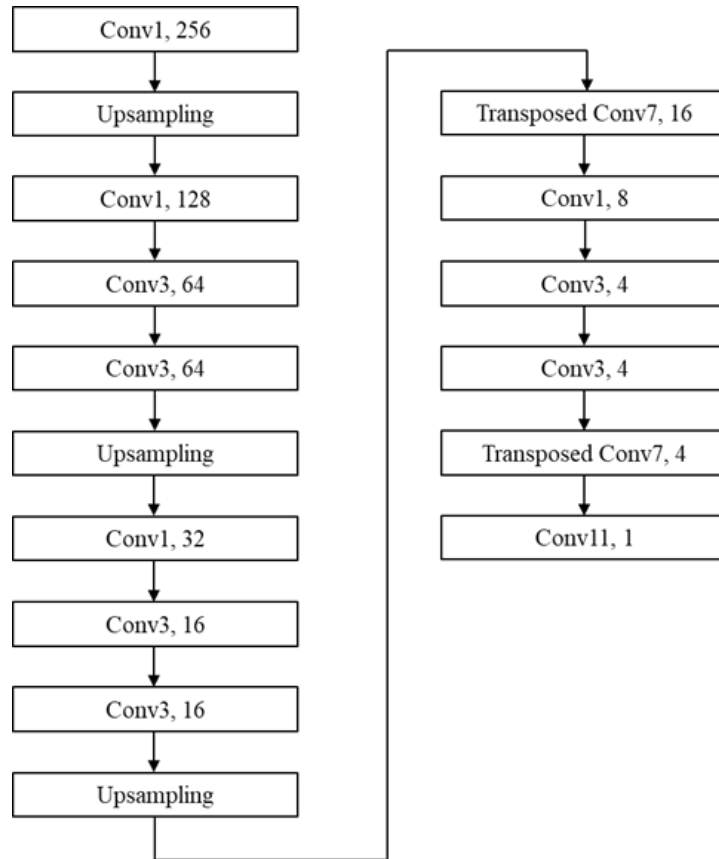
Figure 2.6. The structure of the deep model.

Figure 2.6 shows the structure of a deeper model constructed by replacing some

strided transposed convolutional layers with stacks of 3 convolutional layers and 1 up-

sampling layer. In the following context, the original model is called the "shallow

model", and the deeper model is called the "deep model". The shallow model has 5

layers, while the deep model has 16 layers. Because each convolutional layer is followed

by a LeakyRelu activation layer, the deeper model has more nonlinearities than the

shallow model. The shallower model has 1,560,641 parameters in total, while the deep model has 1,041,409 parameters.

	Shallow model	Deep model	Improvement
Error in average aspect ratio	5.77%	7.69%	-33.28%
Error in average grain size	8.90%	1.73%	80.56%
Error in grain size std	18.92%	4.05%	78.59%

Table 2.1. Comparison between the deep model and the shallow model.

The deeper model shows a great improvement in performance. Table 1.1 shows the mean aspect ratio, average grain size, and grain size standard deviation of the real micrographs, the predicted micrographs from the shallow model, and the predicted micrographs from the deep model. The deep model has 7.69% relative error in mean aspect ratio, which is slightly higher than the shallow model (5.77%). It implies that using the strided transposed convolutional layer to let the model learn its own spatial up-sampling method can benefit the model to learn low-level geometric features. The deep model has 1.72% relative error in average grain size and 4.05% relative error in grain size standard deviation, where the shallow model has 8.90% relative error in average grain size and 18.92% error in grain size standard deviation. The deep model shows a great improvement in predicting high-level abstract features, especially the high order feature (standard deviation). This observation coincides with the experience that the depth of the model promotes the model's capability of extracting and disentangling high-level features because there are more nonlinear activation layers.

In summary, the deep model has better performance than the shallow model, while the number of parameters is 33.27% less. Thus, the deep model will be used for further investigation.

2.3.3 Number of training epochs

the number of training epochs, or how many times the algorithm is trained, is an important hyperparameter that can greatly affect the model's performance. If a model is trained with an inadequate number of epochs, the GAN model cannot reach a Nash equilibrium state where the generator appreciates the distribution of the real data and generates plausible images. Training a model with an excessive number of epochs also raises two problems. First, it may take too much time and computational resources to train the model. Second, the model may be overfitting to the training dataset, which results in poor generalizability.
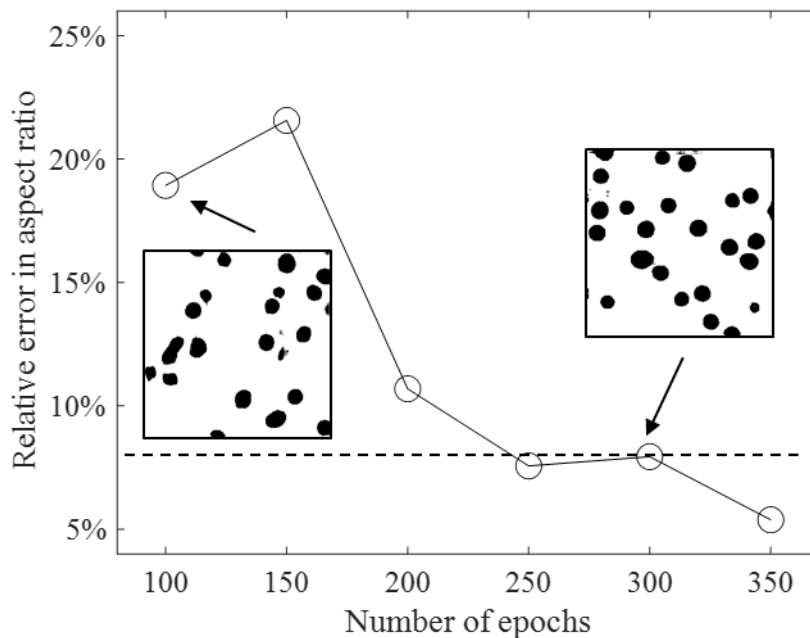
Figure 2.7. Relative error in aspect ratio vs number of epochs.

To quantitatively study the impact of training epochs, the model is trained for 100, 150, 200, 250, 300, and 350 epochs and the predicted accuracy is quantitatively evaluated. In Figure 2.7, the relative error of aspect ratio change against the number of epochs is plotted. When the model is only trained for 100 epochs, the generated grains are elongated ill-shaped. As the training goes, the grain become rounder and rounder and the error in aspect ratio quickly drops.
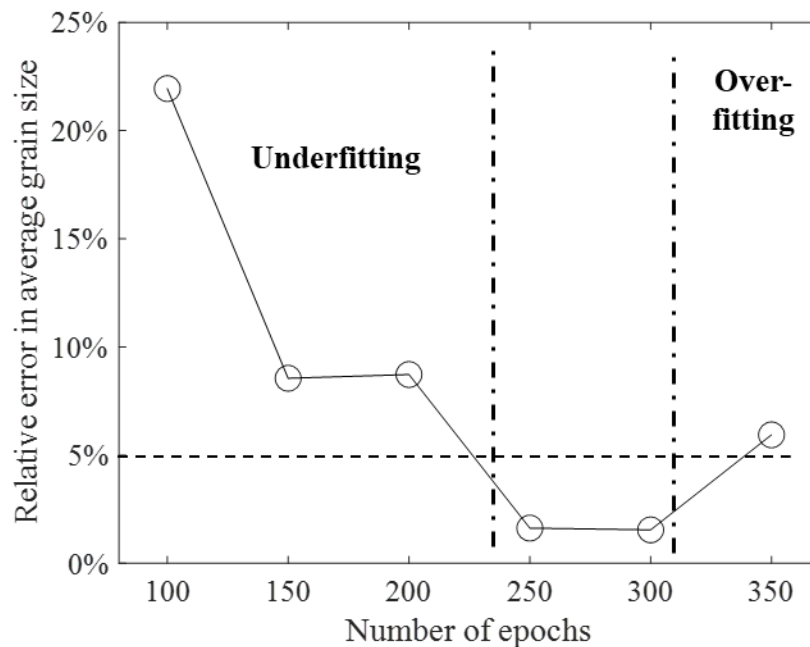
Figure 2.8. Relative error in average grain size vs number of epochs.

Figure 2.8 shows the relative error in average grain size changes with the number of epochs. When the number of epochs increases from 100 to 250, the error quickly drops. However, when the number of epochs increases from 300 to 350, the error increases. A similar trend is observed in Figure 2.9, where the relative error in grain size standard deviation is plotted against the number of epochs. This is because when the number of epochs is smaller than 250, the model is underfitting, which means that the

model has not fully grasped the relationship between the processing parameter λ and the corresponding micrographs. When the number of epochs is larger than 300, the model overfits to the training set and loses some generalizability. In summary, the best number of training epochs is between 250 and 300.
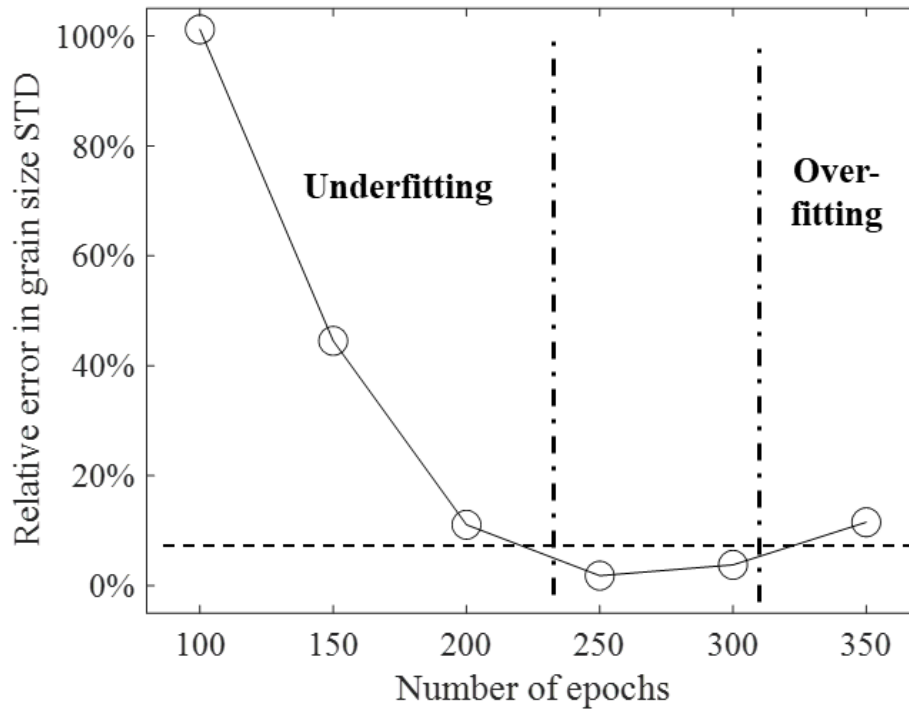
Figure 2.9. Relative error in grain size standard deviation vs number of epochs.

2.3.4 Training set size

The size of the training set is always the critical hyperparameter that determines the model's performance. The success of deep learning algorithms has largely depended on the vast amount of data accumulated on the Internet in the past few decades. Usually, with a larger amount of training data, the model performs better. However, microstructure data has to be acquired through SEM, which is time-consuming and expensive. Trying to boost the model's performance by feeding it more data is not always practical because it could take hundreds of hours and cost much money.
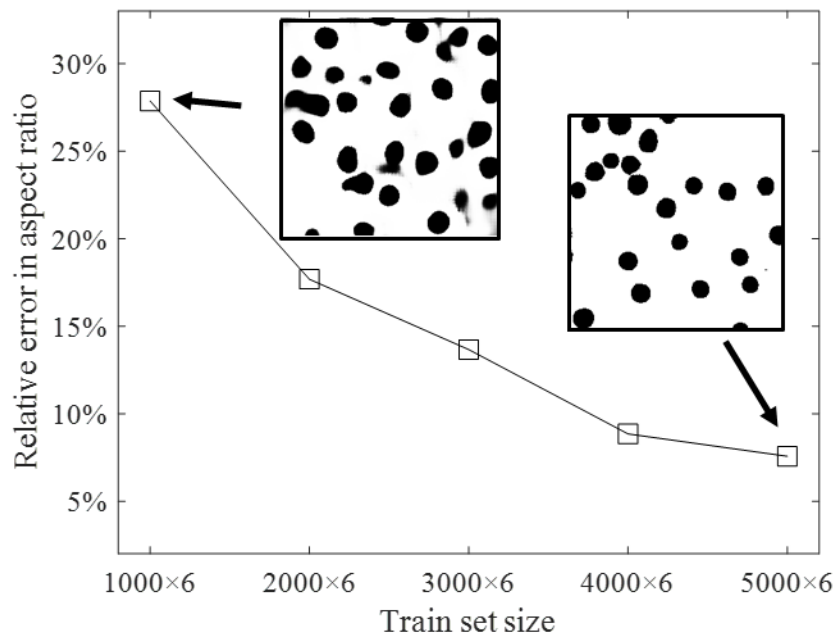
Figure 2.10. Relative error in aspect ratio vs train set size.
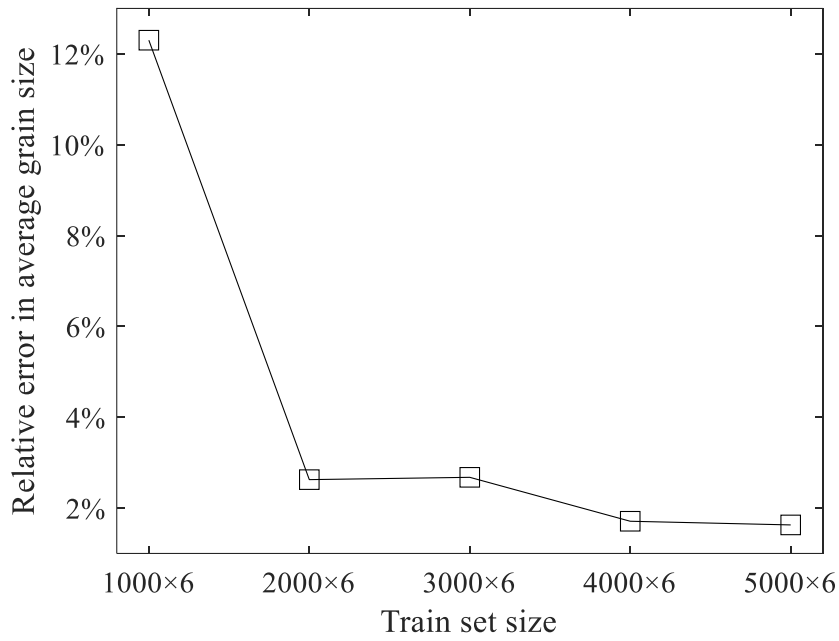
Figure 2.11. Relative error in average grain size vs train set size.
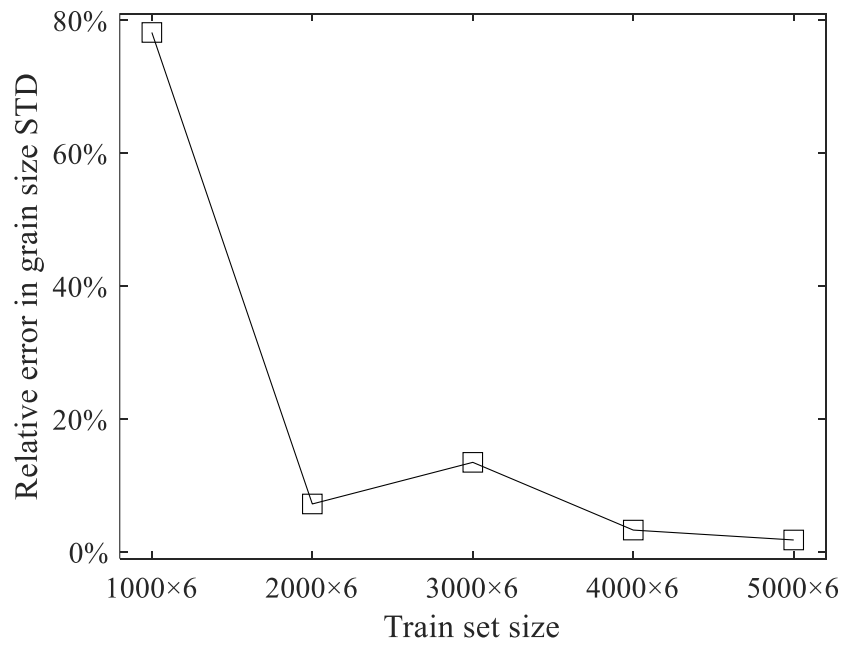
Figure 2.12. Relative error in grain size standard deviation vs train set size.

The number of training samples is changed to study the impact of train set size. The number of training samples in each subset varies from 1,000 to 5,000. Because there are six subsets in the train set, the total number of training examples varies from 6,000 to 30,000. Each time the model is trained, 1,000 micrographs are predicted, and the prediction accuracy is shown in Figure 2.10, Figure 2.11, and Figure 2.12.

As shown in Figure 2.10, Figure 2.11, and Figure 2.12, the prediction accuracy improves as the number of training samples increases. By increasing the number of training samples from 6,000 to 30,000, the relative error in aspect ratio gradually improves from 28% to 8%. The relative error in average grain size decreases from 12% to 3% rapidly when the number of training samples increases from 6,000 to 12,000. Further increase in the number of training samples only improves the relative error in average grain size from 3% to 2%. The same trend is observed in Figure 2.12. These observations suggest the training set size has to be larger than 12,000. However, further increase in the number of training samples may not be worth the time and resources.

2.4 Conclusion

The viability of using a GAN to regress microstructure against a processing parameter and make predictions is demonstrated on a synthetic micrograph dataset. The algorithm is named as Regression-based Wasserstein Generative Adversarial Network (RCWGAN) because it uses Wasserstein distance as its loss function. The impact of different hyperparameters is studied. A deeper model can outperform a shallow model, especially when high-level features are concerned. The number of training epochs greatly influences prediction accuracy. Underfitting and overfitting are identified. The best

number of epochs is between 250 to 300. The impact of train set size is studied. It is found that the number of training examples needs to be larger than 6,000 to ensure good performance. Further increase in the number of training examples leads to a moderate improvement.

CHAPTER THREE

**PREDICTING LASER-SINTERED ALUMINA'S MICROSTRUCTURE BASED
ON LASER POWER**

In this chapter, the RCWGAN is validated to model the relationship between laser power and the microstructure. Some laser-sintered alumina samples are fabricated under different laser powers. SEM micrographs are obtained from those samples to establish a dataset. The RCWGAN is trained on the dataset and then used to predict microstructures corresponding to a laser power that does not appear in the training set. The prediction is accurate after being qualitatively compared with the experimental results.

3.1 Laser sintering alumina

Alumina is an important ceramic material that has excellent mechanical properties, high thermal conductivity, chemical inertness, and high electrical resistivity. Its application ranges from biomedical material [80] to insulators in nuclear fusion reactors [81].

Conventionally, alumina products are fabricated using electrical furnace sintering. Plenty work has been done to study the sintering behavior of furnace sintered alumina [82, 83]. These studies suggest that low heating rate of electrical furnace results in an extensive grain growth, which reduces the mechanical strength of alumina products. In the meantime, electrical furnace sintering also consumes a huge amount of electrical power and takes a long time.

In the laser sintering process, materials are rapidly heated cooled when the laser beam comes across, which gives a high heating rate that can suppress grain growth.

Deckers et. al. used a laser to sinter pre-densified alumina green bodies at elevated temperatures [84]. With a laser power of 2 W, they were able to sinter the alumina sample to 85% density. Fayed et al. studied the effect of laser sintering parameters on the microstructure and physical properties. They demonstrated that a minimum porosity of 4.34% and micro-hardness of 1682 Hv could be reached [85]. Xiao et al. showed that laser sintered alumina had significantly suppressed grain size while the overall density can be as high as 98% [17].

Studying the process-microstructure relationship in the laser sintering process is not easy. The knowledge accumulated from furnace sintering practice no longer works because of the huge difference in heating rate. Physics-based modeling is complicated because many sintering mechanisms exist simultaneously, such as sintering, melting, vaporization, thermomechanical shock, and plasma formation [62, 63, 64]. On the other hand, machine learning-based methods have shown their potential in predicting microstructures quickly and accurately based on processing parameters. This can expedite the material research and design to the next level. In the meantime, we recently demonstrated an approach that can produce a large amount of microstructure data through high-throughput experiments [65]. It can potentially solve the main challenge of machine learning methods: how to get enough data for training.

3.2 Laser sintering system
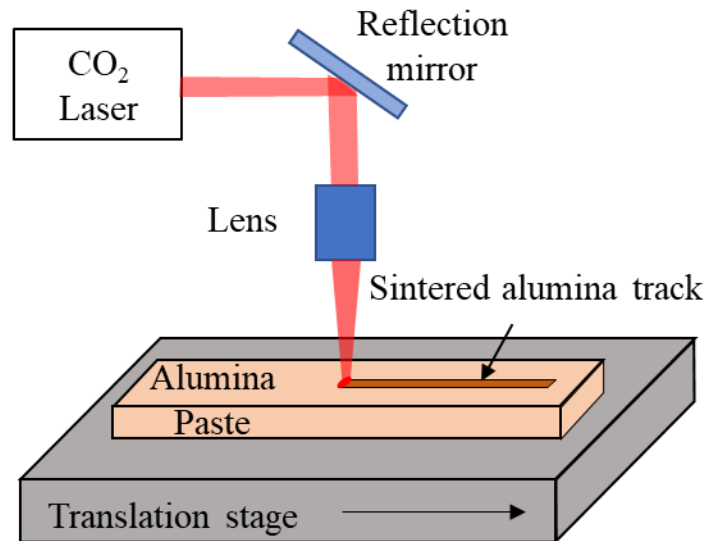
Figure 3.1. Schematic of the laser sintering system

A schematic of our laser sintering system is shown in Figure 3.1. The laser sintering system consists of a z stage, an x-y translation stage, a carbon dioxide laser, and optics that help deliver the laser beam. The laser beam from the carbon dioxide laser (firestarv20, wavelength 10.6 μm, SYNRAD, Inc.) was focused by a ZnSe lens after being delivered by the optics. The lens was mounted on the z stage so that the height of the lens can be adjusted to defocus the laser beam. The translation stage carried the sample to move under the laser spot with a controllable speed.

In this laser sintering system, mainly three processing parameters can be controlled: laser power, scanning speed, and defocusing distance. Laser power determines how much energy will be deposited onto the sample. Scanning speed controls

how long the laser spot stays on a single point. And the defocusing distance controls the size of the laser spot and its energy distribution when it hits the sample surface.

3.3 Laser sintering alumina procedure and result

Alumina paste was prepared before laser sintering. 79.7 wt.% Al2O3 powder (Almatis A152SG, d_{50} = 1.2 μm, Purity: 99.8%, with 0.07% MgO as the sintering aid) and 0.1 wt.% dispersant (Darvan 821A) was mixed with 20.0 wt.% deionized water. The suspension was ball-milled for 48 hours to ensure that alumina particles were uniformly distributed in the water without aggregation. Then, 0.2 wt.% polymer binder (hydroxypropyl methyl cellulose) was added into the suspension slowly while the mixture was mechanically blended by a vacuum mixer for 1 hour. As a result, an alumina paste with appropriate viscosity and green density (~56%) was obtained.

The paste was then deposited on a silica substrate using a doctor blade. The thickness of the film was about 500 μm. After drying for 24 hours, the carbon dioxide laser was used to sinter the alumina paste. The sample was placed onto the laser sintering system described in 3.1. The translation stage carried the sample to move under the laser spot with 0.1 mm/s speed for 50 sec. As a result, a track of laser-sintered alumina with a length 5 mm was fabricated. We varied laser power from 1.4 W to 1.9 W to fabricate 6 lines of laser-sintered alumina.

The microstructures of laser-sintered alumina under different laser powers were characterized using an SEM (Hitachi S4800, Hitachi, Ltd.). For each laser power, we took eight SEM images at different locations along the center of the laser-scanned track.

The magnification is kept as 2000X. Each image had 896×1280 pixels. To increase the

SEM dataset size, we segmented the SEM images into smaller images of 128×128 pixels.

This segmentation size was carefully chosen. If it was too large, the number of samples

would be insufficient for training. If it was too small, there would be an insufficient

number of grains in each small image, making the dataset unrepresentative of the

microstructure features, such as grain size, porosity, and relative density. After

segmentation, there were 560 images for each laser power. To further augment the

dataset, we rotated every image by 90, 180, and 270 degrees so that the number of images

was quadrupled. This image augmentation not only increased the number of samples but

also prevented the algorithm from overfitting [79].
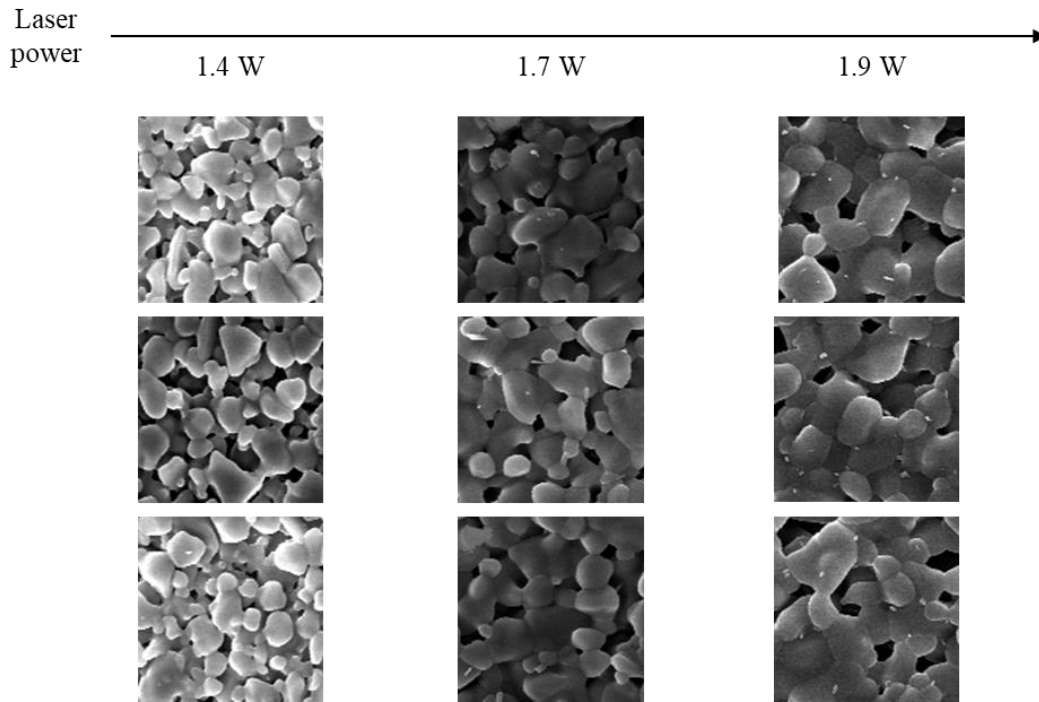
Figure 3.2. Micrographs of alumina sintered by different laser powers.

Some SEM micrograph examples corresponding to different laser powers are shown in Figure 3.2. A strong correlation between the microstructure and the laser power can be observed. From left to right, as the laser power increases, the particles become larger, and the porosity decreases.

3.4 Predicting the microstructures under a new laser power

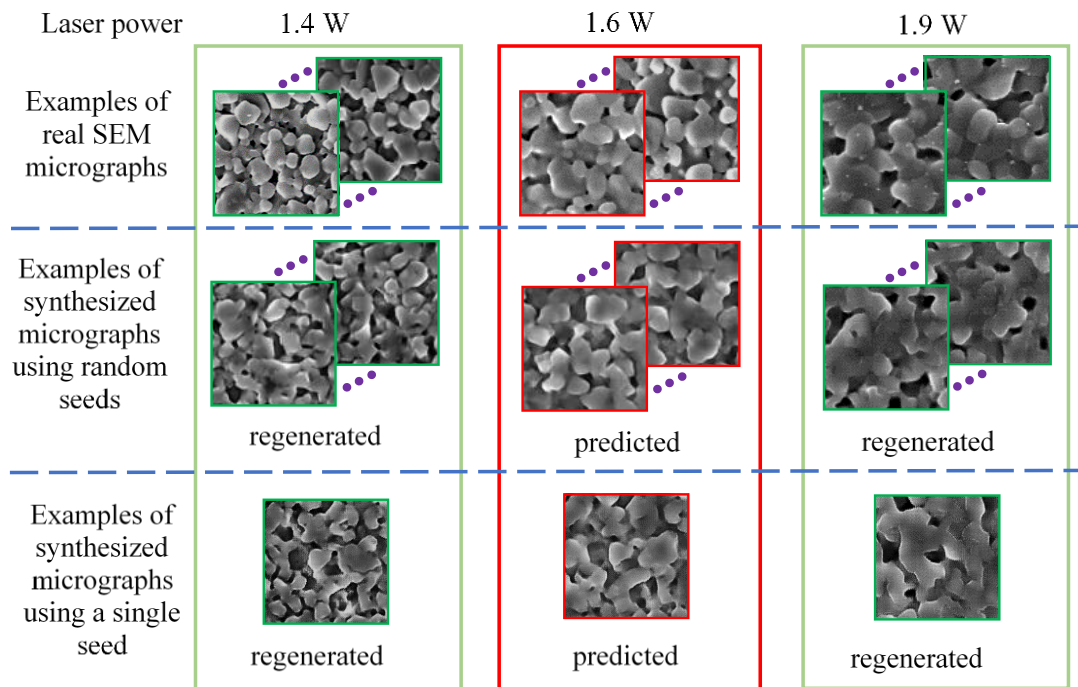*Figure 3.3. The examples of regenerated and predicted SEM micrographs using the RCWGAN.*

The entire SEM micrograph dataset contains 6 subsets corresponding to 6 different laser powers. Five of them whose laser powers were 1.4 W, 1.5 W, 1.7 W, 1.8 W, and 1.9 W formed the training set, while the other one whose laser power was 1.6 W was used for testing. To avoid ambiguity, we call the micrographs that were synthesized

39

using the RCWGAN under the trained conditions, 'regenerated' micrographs. We name the micrographs synthesized under new or unexplored processing conditions, 'predicted' micrographs.

A qualitative comparison among the 'regenerated', 'predicted', and real micrographs is shown in Figure 3.3. The predicted SEM micrographs at 1.6 W laser power faithfully imitate the real SEM micrographs in many aspects of microstructural features, such as particle geometry and relative density. These key microstructural features are very important to predict the material properties in future studies. In addition, the predicted microstructure features also accurately reflected the trend of the influence of laser power. In our previous study, we showed that a higher laser power resulted in larger particle size, larger relative density, and lower porosity [17]. The predicted SEM micrographs under 1.6 W of laser had particle size and relative density that are clearly larger than those of 1.4 W but smaller than those of 1.9 W. We examined both situations of synthesizing SEM micrographs using random seeds and single seed. When random seeds were used, the synthesized SEM micrographs showed similar microstructure features for one laser condition. We explored the latent space of the generated images to rule out the possibility of image generation as a result of "memory effect". As shown in Figure 3, when we use a single seed to synthesize SEM micrographs, the regenerated and predicted images morph continuously from one microstructure to the other, indicating that the laser power-microstructure relationship is indeed "learned" by the neural network.
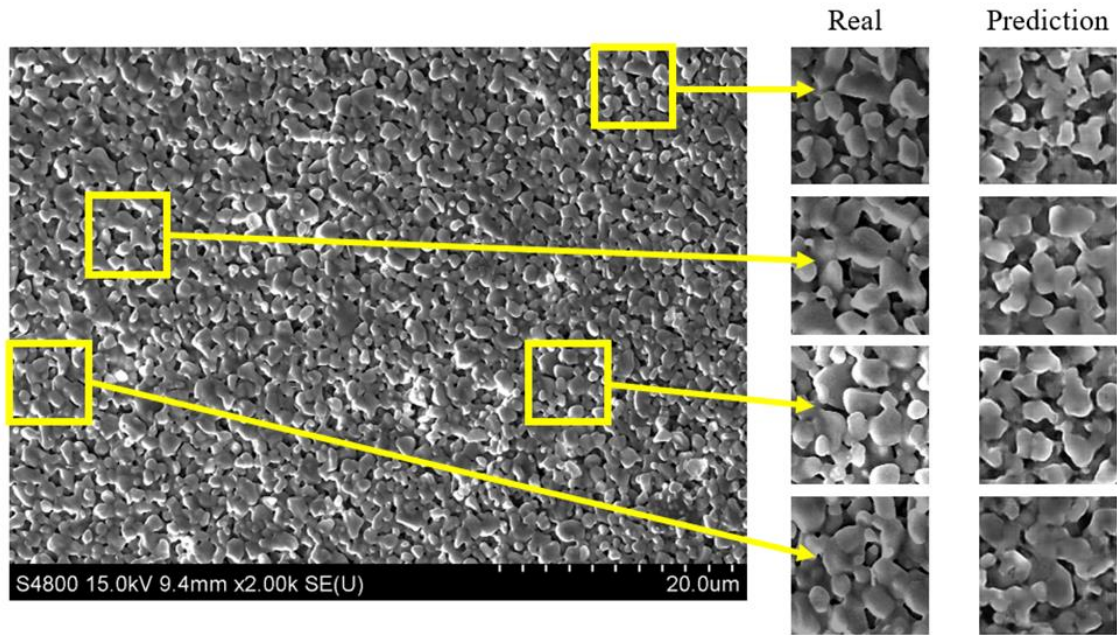
Figure 3.4. The large domain SEM image of an alumina sample sintered under 1.6W, with small domain of SEM magnified from the large one and the corresponding predicted SEM images using the RCWGAN.

It is worth noting that even within one experimentally obtained SEM micrograph, there are variations in the microstructure at different locations. We found that the RCWGAN can also predict such microstructural variation, as shown in Figure 3.4. On the left side of Figure X is a full-size real SEM micrograph of laser-sintered alumina at 1.6 W. Several segmented images of 128×128 pixels are extracted from the full-size SEM micrographs as representatives. On the right to the column of real image segments are the predicted images using RCWGAN from random seeds. This variation is an important characteristic of laser-sintered ceramics as a result from the nature of the laser sintering process. In our training datasets of the laser power of 1.4 W, 1.5 W, 1.7 W, 1.8 W, and

1.9 W, we observed microstructure variation. This is the reason that the predicted results

also present this microstructural variation, which was learned from the training data.

Apart from the visual similarity, it is another piece of evidence that the RCWGAN is

capable of predicting microstructures under unexplored values of a processing parameter.

3.5 Conclusion

In this chapter, the RCWGAN developed in chapter two is applied to a real

micrograph dataset obtained from laser-sintered alumina. With different laser power,

distinct microstructures are experimentally obtained. The RCWGAN regresses the

microstructure against laser power and predicts microstructures under an unseen laser

power. The importance of the loss function is revisited. The impact of two different

regularization methods are studied. With weight clipping, the predicted microstructure

loses many details. With gradient penalty, the predicted microstructure is close to the

experimentally obtained ones.

CHAPTER FOUR

DEEP LEARNING-BASED IN-SITU MICROSTRUCTURE MONITORING

4.1 In-situ monitoring system and surface emission

The RCWGAN is potentially a powerful tool for the real-time monitoring of microstructure during laser-based advanced manufacturing. By recognizing the correlation between the in-situ sensing signals and microstructures, the RCWGAN can make accurate predictions. In addition, the trained RCWGAN consumes relatively low computational power, which makes them potent to be integrated into the fabrication process for real-time microstructure monitoring. Here, I demonstrate in-situ microstructure monitoring by predicting microstructures based on in-situ captured surface emission brightness using the RCWGAN.

Figure 4.1 shows the schematic of the laser sintering system with an in-situ monitoring camera. A carbon dioxide laser with a wavelength of 10.6 μm was used as the energy source for sintering. The laser beam was delivered by a reflection mirror and focused into a line-shape beam by a cylindrical ZnSe lens. The focus distance of the lens was 25.4 mm. At a distance of 30 mm from the focal point, the laser beam projected an elongated elliptical spot on the sample. The length of the ellipse was about 18 mm, and the width was about 4 mm. The power of the laser was set at 46 W. The casted BCZYYb

tape was carried by a translation stage to scan through the laser beam. The scanning speed was kept at 0.1 mm/s.

Figure 4.1. Schematic of the laser-based advanced manufacturing system with an in-situ monitoring camera.
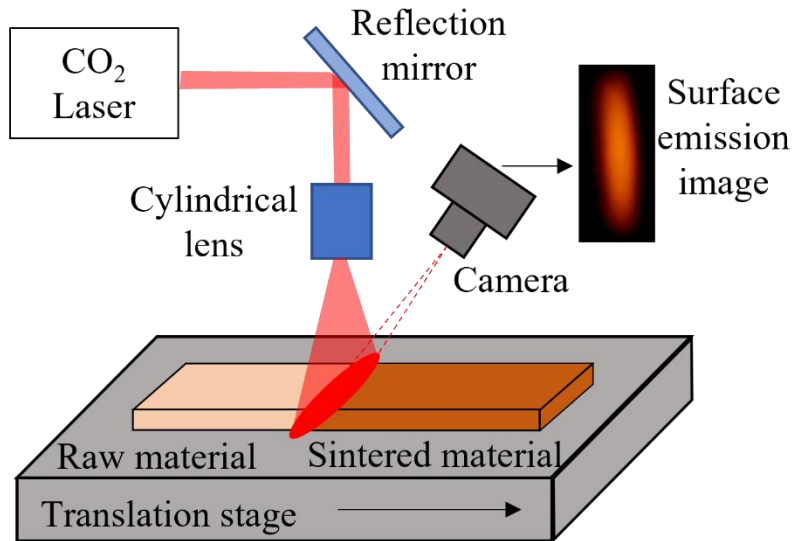
Surface emission images were in-situ captured using a camera (Canon EOS 90D). The camera was set up in an off-axial manner. It aimed at the sintering spot with about 50° relative to the vertical axis. The camera was fixed to the table, and the view angle did not change when the translation stage moved. The ISO sensitivity of the camera was 100, the shutter speed was 1/12500 seconds, and the aperture was 1/25. Under these settings, the camera was not saturated at the strongest thermal radiation. The images recorded by the camera had 1080×1920 pixels, and the speed of recording was 30 frames per second. The camera was synchronized with the translation stage so that the laser sintering spot positions could be accurately correlated with the sample positions for SEM micrographs.

The surface-emission images are not direct measurements of the temperature. The camera uses a silicon-based sensor with an infra-red filter in front of it. It is difficult to infer the surface temperature based on the spectral recording of the camera, because we cannot accurately measure the surface temperature during laser sintering. In this study, we will directly correlate the brightness of the surface-emission image to the microstructure using the RCWGAN.

4.2 Laser sintering experimental procedure

4.2.1 Material preparation

We used BCZYYb with 1% NiO addition as the material for study. The powder pastes of the BCZYYb with NiO additive were prepared using ball-milling of the raw materials powders of $BaCO_3$ (Alfa Aesar 99.8%), Fe_2O_3 (Alfa Aesar 99.9%), CeO_2 (Alfa Aesar 99.9%), ZrO_2 (Alfa Aesar 99.7%), NiO (Alfa Aesar Ni 78.5%), Y_2O_3 (Alfa Aesar 99.9%), and Yb_2O_3 (Alfa Aesar 99.9%)] for 48 h in the stoichiometric ratio, followed by mixing of the ball-milled powder with water, dispersant (DARVAN), and binder (HPMC), as reported in [87].

A green anode ceramic film was processed using direct ink writing (DIW) on a fused silica substrate. The thin film with a uniform thickness of about 500 μm was deposited and dried in the ambient atmosphere for 24 h. The detailed anode layer processing is described in our previous paper [87]. A thin electrolyte layer (BCZYYb with 1 wt.% NiO addition) was deposited on the printed anode film by spray coater. The thickness of the electrolyte layer was about 20 μm. The detailed spray coating processing is described in our previous paper [87].

4.2.2 SEM image acquisition

After the BCZYYb film was sintered by the CO2 laser, the microstructure of the sample at specific positions was characterized using a scanning electron microscope (SEM Hitachi S4800). Seven sampling positions on the surface were selected. Each sampling point was a 500×500 μm^2 square. At each sampling position, five non-overlapping SEM micrographs of the same microstructure were taken.

The collected SEM micrographs (896×1280 pixels, grayscale image) were segmented into smaller ones to increase the size of the training set. The size of one segmented image was 128×128 pixels. Two adjacent segments overlap with each other by half. After segmentation, one full-size SEM micrograph became 247 smaller micrographs. Furthermore, every small micrograph is rotated by 90, 180, and 270 degrees so that the size of the training dataset was quadrupled. This image augmentation not only increases the number of samples but also prevents the algorithm from overfitting [79].

4.3 Correlation between surface emission and microstructure

4.3.1 brightness calculation

An example of an in-situ captured surface emission image is shown in Fig. 4.2. The bright spot was 18 mm long and 4mm wide, which coincided with the shape of the laser spot. A 5×5-pixel square at the center of the bright spot was cropped and extracted, as shown in Figure 2 (a). The actual size of the square was 500×500 $\mu m2$, matching the size of the SEM sampling positions. The pixel values were averaged to calculate the mean brightness of the square in order to reduce noise. The result was divided by 255 for

normalization. As such, a brightness feature was extracted from each surface-emission image. This brightness value ranged from 0.51 to 0.73 among the collected data.

Figure 4.2. Illustration of brightness calculation.
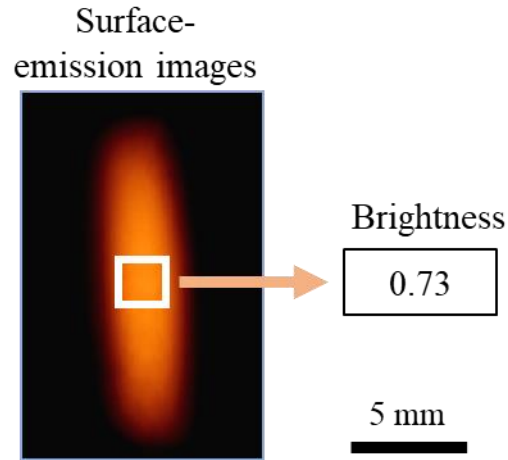
4.3.2 Average grain size calculation

The average grain sizes are measured from a micrograph using the standard ASTM E112 method [88]. This standard is suitable for the grain size characterization for randomly oriented, equiaxed grains. The average grain size was calculated based on the number of grains per unit area for a specific SEM magnification. Specifically, one individual micrograph in a training set had a size of 128×128 pixels. As one pixel corresponds to 0.1 μm, the size of the micrograph can be interpreted as 163.84 μm^2. Then the average grain size was calculated based on ASTM E112.

4.3.3 Qualitative and quantitative evaluation of the relationship between the brightness and microstructure

    As the laser spot moves on the sample surface from left to right, the brightness of the ellipse varies, as shown in Figure 4.3. It suggests that the sintering temperature changes at different positions, although the laser power and scanning speed are set to be the same. The reasons behind this variation could be manifold [84]. Laser instability could be one of the causes. High-power carbon dioxide lasers are inevitably unstable due to passive Q-switch pulsation [89] and thermal instability. Insufficient heat dissipation through the baseplate could be another reason [90]. Identifying the actual cause of the surface color change is beyond the scope of this dissertation.
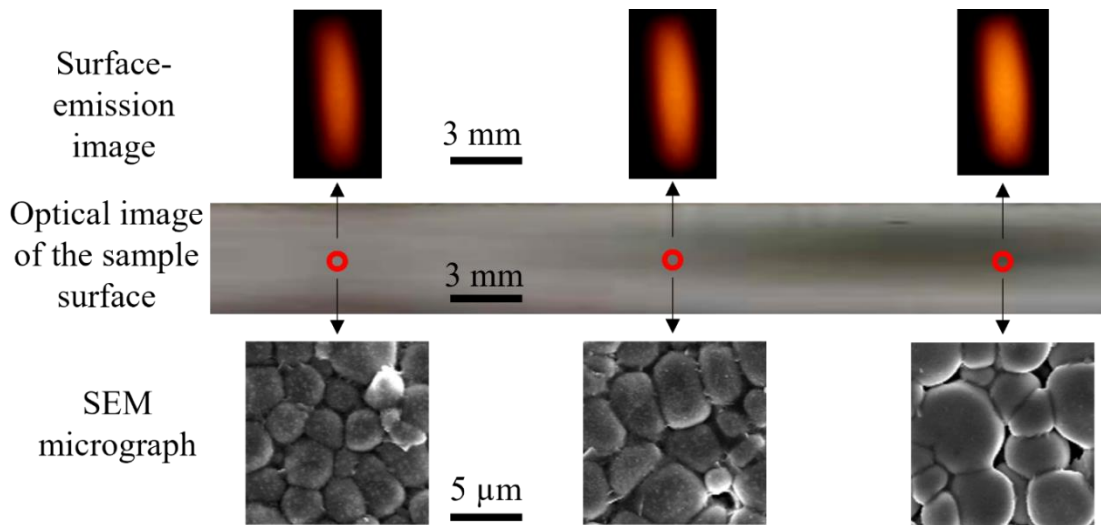
Fig 4.3. Qualitative evaluation of the correlation between the surface-emission images and microstructure.

    Microstructure variation is quantitatively measured by variation of the average grain size. 20 micrographs are randomly selected for each subgroup. The mean and the standard deviation are calculated from the average grain sizes of the 20 micrographs. The

results are plotted against brightness values in Figure 4.4. When the brightness increases

from 0.51 to 0.67, the average grain size grows from 2.29 μm to 2.74 μm. The further

increase in the brightness on longer changes the average grain size significantly.
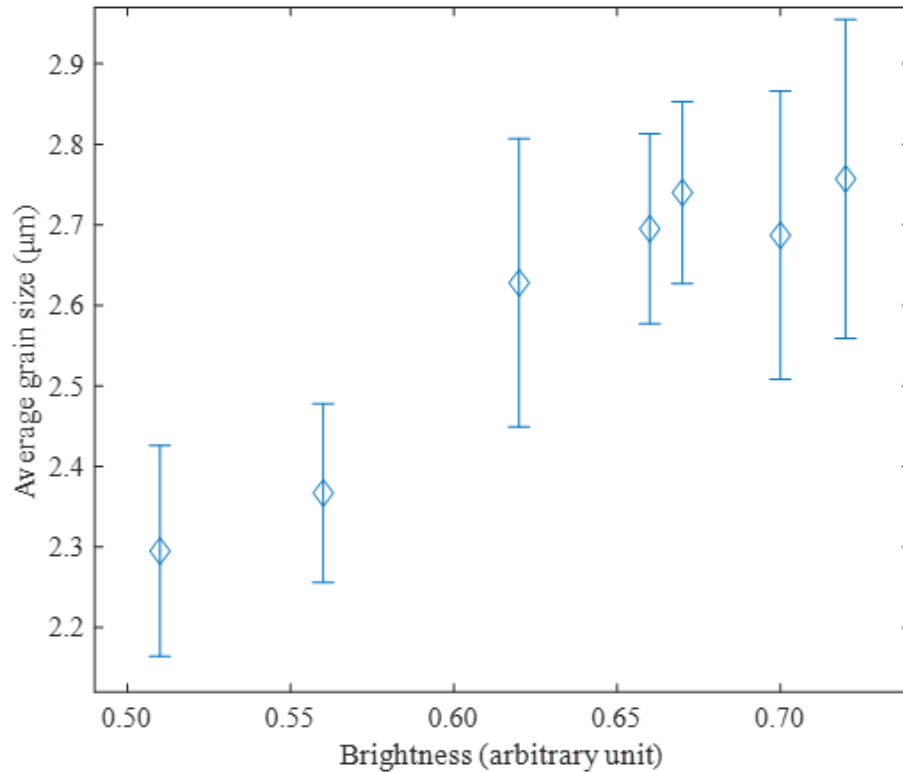
Figure 4.4. Average grain size vs. brightness.

4.4 Predicting microstructure with the RCWGAN

After training, the RCWGAN can produce high-fidelity images corresponding to

the input brightness value. Several synthesized micrographs and experimentally obtained

ones are shown in Figure 4.5 as examples. The brightness values 0.56 and 0.72 are in the

training set. The micrographs synthesized from these brightness values are called

"regenerated" micrographs in this paper. The micrographs synthesized from the unknown

brightness value 0.66 are called "predicted" micrographs in this paper because the

brightness of 0.66 is not in the training set. The synthesized micrographs were similar to the real ones under the same brightness value, in terms of grain size and grain shape. This is true for both "regenerated" and "predicted" micrographs.
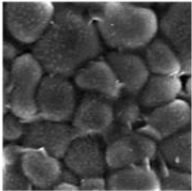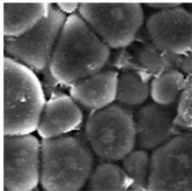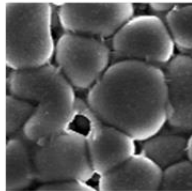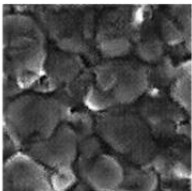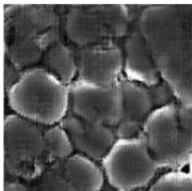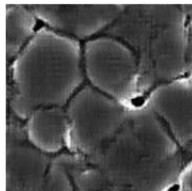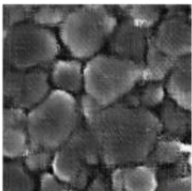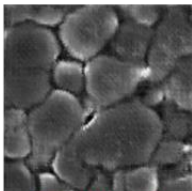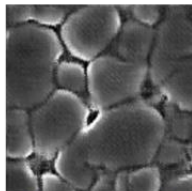
Figure 4.5. Examples of regenerated and predicted SEM micrographs using the RCWGAN.

In the synthesized micrographs with random seeds, from left to right in Figure 4.5, the grain size increases as the brightness value increases. This fits the experimental trend very well, since normally, a higher brightness corresponds to a higher sintering temperature. The ceramics normally have a larger grain size under a higher sintering temperature.

50

To better show the trend of microstructural features over the increasing brightness values, the micrographs synthesized with a fixed seed are shown at the bottom of Figure 4.5. Because the seed is fixed, some microstructure features like the spatial distribution of the grains are also fixed, which is the reason why they look much alike. From 0.56 to 0.66, a clear increase in the grain size can be seen. From 0.66 to 0.72, the grain size does not change too much. This coincides with the trend we observe in Figure 20. In summary, the synthesized micrographs are highly similar to the real ones, and the relationship between the brightness value and the grain size is clearly learned by the algorithm.

To quantitatively measure the algorithm's accuracy, average grain sizes are calculated on the synthesized micrographs and compared with the average grain sizes measured on the real micrographs for the same brightness. 20 micrographs under each brightness value are synthesized. The average grain sizes are measured and plotted in Figure 4.6.

The average grain sizes of synthesized micrographs are close to the real ones. The mean absolute error is 0.05 μm for the "regenerated" micrographs. The real average grain size of the validation set is 2.70 μm, while the predicted average grain size is 2.58 μm. The absolute error is 0.12 μm, which is 4.5% of the real average grain size. From left to right, the average grain size of the synthesized micrographs follows the same trend as the real average grain size. When the brightness increases from 0.52 to 0.67, the average gran size grows quickly. After the brightness exceeds 0.67, the average grain size hardly changes. These results suggest that the RCWGAN grasps the relationship between the brightness and the micrograph. It is able to make accurate predictions in terms of the

average grain size. The performance of the algorithm can be further improved by providing it with more training data.
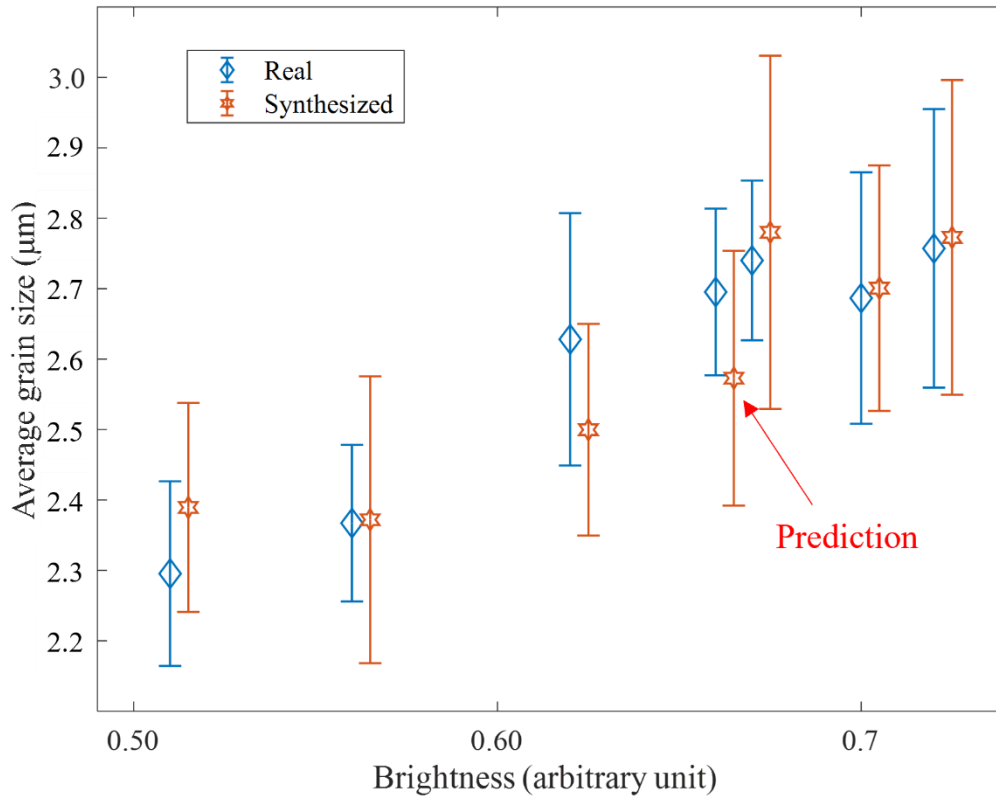
Figure 4.6. Average grain sizes of the real micrographs and the synthesized ones.

4.5 Model computation time

The trained model can generate authentic micrographs in a short time. When the model runs on a desktop computer, it can generate 10 micrographs in 1.05 seconds with 4 CPUs (Intel Core i5-7600K). It is comparable with the speed of the monitoring camera, which is 30 frames per second. Thus, our trained model is capable of in-situ microstructure monitoring based on the brightness of surface emission.

52

4.6 Conclusion

In this chapter, in-situ monitoring microstructure using the RCWGAN is proposed

and demonstrated. An in-situ monitoring that uses a camera to capture surface emission is

built. The correlation between the surface emission brightness and the corresponding

microstructure is demonstrated. After the RCWGAN learns the correlation, it is used to

predict a microstructure under an unseen brightness value. The predicted microstructure

is accurate when compared with the real one in terms of average grain size.

CHAPTER FIVE

CONCLUSION

5.1 Brief summary

The traditional practice of establishing process-microstructure relationships to guide material fabrication is trial-and-error experiments. It is slow at every step. The fabrication process, furnace sintering for example, takes hours or even days to complete. The microstructures of the fabricated samples are characterized by SEM, which takes hours and costs hundreds of dollars for each sample. The obtained microstructure data are analyzed by experts to find the correlation between the process parameters and the microstructures. It also takes hours to complete.

The material development cycle can be accelerated by accurately predicting the microstructure based on processing parameters. When the laser-based advanced manufacturing technology has expedited the fabrication process from hours to minutes, it is highly desirable to fasten the pace in microstructure characterization and analysis. Microstructure prediction can potentially save time in these steps. However, current microstructure prediction methods face their own challenges. Physical-based modeling is computationally expensive. Even with a high-performance computing cluster, a simulation could take hours to complete. Feature-based machine learning methods consume much less computational power. Nevertheless, these approaches require extracting features from microstructures, which inevitably leads to information loss. Besides, there is no well-established method to analyze complex features in SEM micrographs.

In this dissertation, I propose to regress microstructures against processing parameters and make predictions with a CGAN. In chapter two, a methodology of training, validating, and optimizing a CGAN is developed. A synthetic micrograph dataset with simple microstructure features is established to train the CGAN. After training, the CGAN predicts the microstructure according to an unseen processing parameter value. Aspect ratio, average grain size, and grain size standard deviation are selected as quantitative metrics to evaluate the prediction accuracy. A mathematical explanation why the Wasserstein loss function should be used instead of the Jenson-Shannon divergence is offered. The impact of model depth on the prediction accuracy of features at different levels is studied. In addition, the number of training epochs and size of the train set are studied. Two important conclusions are found. First, there is an optimal number of training epochs. Below that number, the model underfits and fails to fully appreciate the complex relationship between the microstructure and the processing parameter. Above that number, the model overfits the train set and prediction accuracy deteriorates. Second, the size of the train set has to be larger than 2,000 times the number of subsets to ensure good prediction accuracy. However, further increase in the train set size only brings a moderate improvement, which may not be worth the time and resources. In the end, the optimized CGAN algorithm is named as regression-based conditional Wasserstein generative adversarial network (RCWGAN). The RCWGAN can accurately predict microstructures with over 92% accuracy under the quantitative metrics.

In chapter three, the microstructure prediction capability is validated on an SEM micrograph dataset. Two regularization technologies, weight clipping and gradient

penalty, are studied. With weight clipping, the generated microstructure loses many details. With gradient penalty, those details are well preserved. After the RCWGAN is trained, it is used to predict the microstructure corresponding to unseen laser power. The prediction is accurate under qualitative evaluation.

In chapter four, I proposed an in-situ microstructure monitoring method using the RCWGAN. The RCWGAN correlates the microstructure with in-situ monitored surface emission brightness. After training, the RCWGAN can predict the microstructure based on the in-situ monitoring signal in seconds. The prediction is accurate under qualitative and quantitative evaluation. Thus, in-situ microstructure monitoring is realized by integrating the RCWGAN into a laser sintering system. With this capability, it is possible to precisely control the microstructure at any desired location. It enables the fabrication of a new kind of materials with heterogeneous microstructure and consequently novel properties.

In summary, a new concept of using deep learning to predict material microstructures during advanced manufacturing is proposed and demonstrated. The RCWGAN is designed and optimized to accurately predict microstructures, after various hyperparameters are systematically studied on a synthetic micrograph dataset. The prediction accuracy is over 92% using various microstructural features as metrics. Then the RCWGAN is validated by predicting laser-sintered alumina's microstructure as a function of laser power. Then, it is used to realize in-situ microstructure monitoring during laser sintering. After training, the RCWGAN can accurately predict the microstructure based on in-situ monitored surface emission brightness in seconds.

5.2 Innovations and contributions

The major scientific and technical merits of this work include:

1) A new concept of using deep learning to predict material microstructures during advanced manufacturing is proposed. With this new concept, the material development cycle in advanced manufacturing can be accelerated.

2) Two microstructure prediction methods, physical-based modeling and feature-based machine learning, are reviewed. Limitations of them are summarized.

3) Using a conditional GAN to regress microstructures against processing parameters and make predictions is proposed. Related research is reviewed to prove the viability.

4) A methodology of training, validating, and optimizing a CGAN is developed. First, a dataset that consists of many processing parameter-microstructure pairs is established. After the CGAN is trained on the dataset, the microstructure corresponding to an unexplored processing parameter value is predicted. The predicted microstructure is compared with the real one using various microstructural features as metrics. With these quantitative metrics, hyperparameters like loss function are studied and optimized.

5) Various hyperparameters are studied. A mathematical explanation of why the Wasserstein distance should be used as the loss function rather than the Jenson-Shannon divergence is offered. By comparing a deep model with a shallow model, the impact of model depth is quantified. When the number of epochs is studied, underfitting and overfitting are observed, which suggests that the number of epochs should be carefully

chosen. The study of the size of train set leads to the conclusion that for each processing

parameter value, the number of samples should be larger than 2,000.

6) The RCWGAN is validated by predicting laser-sintered alumina's microstructure as a

function of laser power.

7) The laser sintering system is integrated with an in-situ monitoring camera to monitor

surface emission brightness.

8) The correlation between surface emission brightness and microstructure is observed

and quantified.

9) In-situ microstructure monitoring is proposed and demonstrated by accurately

predicting the microstructure based on in-situ monitored surface emission brightness

using the RCWGAN.

5.3 Future work

5.3.1 Multiple processing parameters

In this dissertation, only one processing parameter is considered at a time. In the

synthetic microstructure dataset, a hypothetical processing parameter λ controls the

microstructure. In the laser-sintered alumina's microstructure dataset, laser power is the

parameter of interest. And in the in-situ monitoring case, only brightness is used to

predict the microstructure. However, in laser-based advanced manufacturing, many

processing parameters influence the microstructure simultaneously. To better guide the

fabrication process, the RCWGAN should regress the microstructure against all

processing parameters at the same time. The essential challenge is to establish an

adequate dataset. On the one hand, this dataset should be diverse enough to represent the correlation between every processing parameter and the microstructure. On the other hand, the dataset should not be too large to build. In addition, an imbalanced dataset could deteriorate the RCWGAN's performance.

In summary, to address the challenge of using the RCWGAN to regress the microstructure against multiple processing parameters, two questions need to be answered in future research. The first question is how to design an appropriate dataset. The second question is how to solve the data imbalance problem.

5.3.2 Property prediction

The predicted microstructure can be used to further predict material properties because various of material properties are determined by the microstructure. Several papers that used CNNs to predict material properties based on microstructures have been reviewed in chapter one. Is it possible to use a CNN to predict properties based on the predicted microstructure? To answer this question, three steps will be taken. First, a process-microstructure dataset will be established to train the RCWGAN. Second, a microstructure-property dataset will be built to train a CNN. Third, the microstructure predicted by the RCWGAN will be fed to the trained CNN to predict its properties. The predicted properties will be compared with the experimental results to evaluate the prediction accuracy.

5.3.3 Feedback control

In chapter four, in-situ microstructure monitoring with the RCWGAN is proposed and demonstrated. The next step is to feed microstructure information back to a controller to control the processing parameters so that a predesigned microstructure profile can be fabricated.

APPENDICES

Appendix A

Publication list

1. **Tang, J.,** Geng, X., Li, D., Shi, Y., Tong, J., Xiao, H., & Peng, F. (2021). Machine learning-based microstructure prediction during laser sintering of alumina. Scientific Reports, 11(1), 1-10.

2. Geng, X., **Tang, J.**, Sheridan, B., Sarkar, S., Tong, J., Xiao, H., ... & Peng, F. (2021). Ultra-Fast Laser Fabrication of Alumina Micro-Sample Array and High-Throughput Characterization of Microstructure and Hardness. Crystals, 11(8), 890.

3. Lei, J., Zhang, Q., Song, Y., **Tang, J.**, Tong, J., Peng, F., & Xiao, H. (2020). Laser-assisted embedding of all-glass optical fiber sensors into bulk ceramics for high-temperature applications. Optics & Laser Technology, 128, 106223.

4. Zhang, Q., Lei, J., Chen, Y., **Tang, J.**, Wu, Y., Hua, L., & Xiao, H. (2020). Information integrated glass module fabricated by integrated additive and subtractive manufacturing. Optics letters, 45(7), 1663-1666.

5. Zhang, Q., Lei, J., Chen, Y., **Tang, J.**, Wu, Y., Hua, L., & Xiao, H. (2020, March). Application of glass 3D printing using direct laser melting for fabrication of photonic sensors. In Laser 3D Manufacturing VII (Vol. 11271, p. 112710S). International Society for Optics and Photonics.

6. Zhu, X., Hua, L., Lei, J., **Tang, J.**, Murdoch, L., & Xiao, H. (2021). Microwave–photonic low-coherence interferometry for dark zone free distributed optical fiber sensing. Optics Letters, 46(5), 1173-1176.

References

[1] McDowell, D. L., & LeSar, R. A. (2016). The need for microstructure informatics in process–structure–property relations. MRS Bulletin, 41(8), 587-593.

[2] Valarezo, A., & Sampath, S. (2011). An integrated assessment of process-microstructure-property relationships for thermal-sprayed NiCr coatings. Journal of thermal spray technology, 20(6), 1244-1258.

[3] Masoumi, F., Shahriari, D., Monajati, H., Cormier, J., Flipo, B. C. D., Devaux, A., & Jahazi, M. (2019). Linear friction welding of AD730™ Ni-base superalloy: Process-microstructure-property interactions. Materials & Design, 183, 108117.

[4] Bouwhuis, B. A., Tang, S. K., & Hibbard, G. D. (2008). Process–microstructure–property relationships in AA3003 expanded metal periodic cellular truss cores. Composites Part A: Applied Science and Manufacturing, 39(9), 1556-1564.

[5] Mittemeijer, E. J. (2010). Fundamentals of materials science: the microstructure–property relationship using metals as model systems. Springer Science & Business Media.

[6] Schempp, P., Cross, C. E., Häcker, R., Pittner, A., & Rethmeier, M. (2013). Influence of grain size on mechanical properties of aluminium GTA weld metal. Welding in the World, 57(3), 293-304.

[7] Clark, D., Tong, J., Morrissey, A., Almansoori, A., Reimanis, I., & O'Hayre, R. (2014). Anomalous low-temperature proton conductivity enhancement in a novel protonic nanocomposite. Physical Chemistry Chemical Physics, 16(11), 5076-5080.

[8] Lien, W., Roberts, H. W., Platt, J. A., Vandewalle, K. S., Hill, T. J., & Chu, T. M. G. (2015). Microstructural evolution and physical behavior of a lithium disilicate glass–ceramic. Dental materials, 31(8), 928-940.

[9] Wang, W., Chen, W., Zhang, W., Cui, G., & Wang, E. (2018). Effect of deformation temperature on texture and mechanical properties of ZK60 magnesium alloy sheet rolled by multi-pass lowered-temperature rolling. Materials Science and Engineering: A, 712, 608-615.

[10] Spinelli, J. E., Tosetti, J. P., Santos, C. A., Spim, J. A., & Garcia, A. (2004). Microstructure and solidification thermal parameters in thin strip continuous casting of a stainless steel. Journal of Materials Processing Technology, 150(3), 255-262.

[11] Wang, W., Fu, Z., Wang, H., & Yuan, R. (2002). Influence of hot pressing sintering temperature and time on microstructure and mechanical properties of TiB2 ceramics. Journal of the European Ceramic Society, 22(7), 1045-1049.

[12] Mahmoud, W. E., Al-Agel, F. A., & Al-Arfaj, E. A. (2013). The influence of sintering temperature on the engineered nanoporous titaniaceramics. Materials Letters, 96, 146-148.

[13] Cao, X. J., Jahazi, M., Immarigeon, J. P., & Wallace, W. (2006). A review of laser welding techniques for magnesium alloys. Journal of Materials Processing Technology, 171(2), 188-204.

[14] Kruth, J. P., Wang, X., Laoui, T., & Froyen, L. (2003). Lasers and materials in selective laser sintering. Assembly Automation.

[15] Kruth, J. P., Froyen, L., Van Vaerenbergh, J., Mercelis, P., Rombouts, M., & Lauwers, B. (2004). Selective laser melting of iron-based powder. Journal of materials processing technology, 149(1-3), 616-622.

[16] Yeo, C. Y., Tam, S. C., Jana, S., & Lau, M. W. (1994). A technical review of the laser drilling of aerospace materials. Journal of materials processing technology, 42(1), 15-49.

[17] Geng, X., Hong, Y., Lei, J., Ma, J., Chen, J., Xiao, H., ... & Peng, F. (2021). Ultra-fast, selective, non-melting, laser sintering of alumina with anisotropic and size-suppressed grains. Journal of the American Ceramic Society, 104(5), 1997-2006.

[18] Ghaini, F. M., Hamedi, M. J., Torkamany, M. J., & Sabbaghzadeh, J. (2007). Weld metal microstructural characteristics in pulsed Nd: YAG laser welding. Scripta Materialia, 56(11), 955-958.

[19] Thijs, L., Verhaeghe, F., Craeghs, T., Van Humbeeck, J., & Kruth, J. P. (2010). A study of the microstructural evolution during selective laser melting of Ti–6Al–4V. Acta materialia, 58(9), 3303-3312.

[20] Mu, S., Zhao, Z., Lei, J., Hong, Y., Hong, T., Jiang, D., ... & Tong, J. (2018). Engineering of microstructures of protonic ceramics by a novel rapid laser reactive sintering for ceramic energy conversion devices. Solid State Ionics, 320, 369-377.

[21] Moelans, N., Blanpain, B., & Wollants, P. (2008). An introduction to phase-field modeling of microstructure evolution. Calphad, 32(2), 268-294.

[22] Chen, L. Q. (2002). Phase-field models for microstructure evolution. Annual review of materials research, 32(1), 113-140.

[23] Wang, Y. U. (2006). Computer modeling and simulation of solid-state sintering: A phase field approach. Acta materialia, 54(4), 953-961.

[24] Echebarria, B., Folch, R., Karma, A., & Plapp, M. (2004). Quantitative phase-field model of alloy solidification. Physical review E, 70(6), 061604.

[25] Takaki, T. (2014). Phase-field modeling and simulations of dendrite growth. ISIJ international, 54(2), 437-444.

[26] Li, J. Q., Fan, T. H., Taniguchi, T., & Zhang, B. (2018). Phase-field modeling on laser melting of a metallic powder. International Journal of Heat and Mass Transfer, 117, 412-424.

[27] Zhang, X., & Liao, Y. (2018). A phase-field model for solid-state selective laser sintering of metallic materials. Powder technology, 339, 677-685.

[28] Yang, Y., Ragnvaldsen, O., Bai, Y., Yi, M., & Xu, B. X. (2019). 3D non-isothermal phase-field simulation of microstructure evolution during selective laser sintering. npj Computational Materials, 5(1), 1-12.

[29] Miyoshi, E., Takaki, T., Ohno, M., Shibuta, Y., Sakane, S., Shimokawabe, T., & Aoki, T. (2017). Ultra-large-scale phase-field simulation study of ideal grain growth. NPJ Computational Materials, 3(1), 1-6.

[30] Portugal, I., Alencar, P., & Cowan, D. (2018). The use of machine learning algorithms in recommender systems: A systematic review. Expert Systems with Applications, 97, 205-227.

[31] Maes, S., Tuyls, K., Vanschoenwinkel, B., & Manderick, B. (2002, January). Credit card fraud detection using Bayesian and neural networks. In Proceedings of the 1st international naiso congress on neuro fuzzy technologies (pp. 261-270).

[32] Nassif, A. B., Shahin, I., Attili, I., Azzeh, M., & Shaalan, K. (2019). Speech recognition using deep neural networks: A systematic review. IEEE access, 7, 19143-19165.

[33] AbuShawar, B., & Atwell, E. (2015). ALICE chatbot: Trials and outputs. Computación y Sistemas, 19(4), 625-632.

[34] Memon, J., Sami, M., Khan, R. A., & Uddin, M. (2020). Handwritten optical character recognition (OCR): A comprehensive systematic literature review (SLR). IEEE Access, 8, 142642-142668.

[35] Zhao, Z. Q., Zheng, P., Xu, S. T., & Wu, X. (2019). Object detection with deep learning: A review. IEEE transactions on neural networks and learning systems, 30(11), 3212-3232.

[36] Carleo, G., Cirac, I., Cranmer, K., Daudet, L., Schuld, M., Tishby, N., ... & Zdeborová, L. (2019). Machine learning and the physical sciences. Reviews of Modern Physics, 91(4), 045002.

[37] Schütt, K. T., Gastegger, M., Tkatchenko, A., Müller, K. R., & Maurer, R. J. (2019). Unifying machine learning and quantum chemistry with a deep neural network for molecular wavefunctions. Nature communications, 10(1), 1-10.

[38] Kononenko, Igor. "Machine learning for medical diagnosis: history, state of the art and perspective." Artificial Intelligence in medicine 23.1 (2001): 89-109.

[39] Bock, F. E., Aydin, R. C., Cyron, C. J., Huber, N., Kalidindi, S. R., & Klusemann, B. (2019). A review of the application of machine learning and data mining approaches in continuum materials mechanics. Frontiers in Materials, 6, 110.

[40] Albawi, S., Mohammed, T. A., & Al-Zawi, S. (2017, August). Understanding of a convolutional neural network. In 2017 International Conference on Engineering and Technology (ICET) (pp. 1-6). Ieee.

[41] Yang, C., Kim, Y., Ryu, S., & Gu, G. X. (2020). Prediction of composite microstructure stress-strain curves using convolutional neural networks. Materials & Design, 189, 108509.

[42] Cecen, A., Dai, H., Yabansu, Y. C., Kalidindi, S. R., & Song, L. (2018). Material structure-property linkages using three-dimensional convolutional neural networks. Acta Materialia, 146, 76-84.

[43] Herriott, C., & Spear, A. D. (2020). Predicting microstructure-dependent mechanical properties in additively manufactured metals with machine-and deep-learning methods. Computational Materials Science, 175, 109599.

[44] Hashemi, S., & Kalidindi, S. R. (2021). A machine learning framework for the temporal evolution of microstructure during static recrystallization of polycrystalline materials simulated by cellular automaton. Computational Materials Science, 188, 110132.

[45] Brough, D. B., Kannan, A., Haaland, B., Bucknall, D. G., & Kalidindi, S. R. (2017). Extraction of process-structure evolution linkages from X-ray scattering measurements

using dimensionality reduction and time series analysis. Integrating materials and manufacturing innovation, 6(2), 147-159.

[46] Brough, D. B., Wheeler, D., Warren, J. A., & Kalidindi, S. R. (2017). Microstructure-based knowledge systems for capturing process-structure evolution linkages. Current Opinion in Solid State and Materials Science, 21(3), 129-140.

[47] Goodfellow, I., Pouget-Abadie, J., Mirza, M., Xu, B., Warde-Farley, D., Ozair, S., ... & Bengio, Y. (2014). Generative adversarial nets. Advances in neural information processing systems, 27.

[48] Karras, T., Aila, T., Laine, S., & Lehtinen, J. (2017). Progressive growing of gans for improved quality, stability, and variation. arXiv preprint arXiv:1710.10196.

[49] Karras, T., Laine, S., & Aila, T. (2019). A style-based generator architecture for generative adversarial networks. In Proceedings of the IEEE/CVF Conference on Computer Vision and Pattern Recognition (pp. 4401-4410).

[50] Hamada, K., Tachibana, K., Li, T., Honda, H., & Uchida, Y. (2018). Full-body high-resolution anime generation with progressive structure-conditional generative adversarial networks. In Proceedings of the European Conference on Computer Vision (ECCV) Workshops (pp. 0-0).

[51] Alsaiari, A., Rustagi, R., Thomas, M. M., & Forbes, A. G. (2019, March). Image denoising using a generative adversarial network. In 2019 IEEE 2nd International Conference on Information and Computer Technologies (ICICT) (pp. 126-132). IEEE.

[52] Joshi, A., Cho, M., Shah, V., Pokuri, B., Sarkar, S., Ganapathysubramanian, B., & Hegde, C. (2020, April). InvNet: encoding geometric and statistical invariances in deep

generative models. In Proceedings of the AAAI Conference on Artificial Intelligence (Vol. 34, No. 04, pp. 4377-4384).

[53] Gayon-Lombardo, A., Mosser, L., Brandon, N. P., & Cooper, S. J. (2020). Pores for thought: generative adversarial networks for stochastic reconstruction of 3D multi-phase electrode microstructures with periodic boundaries. npj Computational Materials, 6(1), 1-11.

[54] Li, X., Yang, Z., Brinson, L. C., Choudhary, A., Agrawal, A., & Chen, W. (2018, August). A deep adversarial learning methodology for designing microstructural material systems. In International Design Engineering Technical Conferences and Computers and Information in Engineering Conference (Vol. 51760, p. V02BT03A008). American Society of Mechanical Engineers.

[55] Chun, S., Roy, S., Nguyen, Y. T., Choi, J. B., Udaykumar, H. S., & Baek, S. S. (2020). Deep learning for synthetic microstructure generation in a materials-by-design framework for heterogeneous energetic materials. Scientific reports, 10(1), 1-15.

[56] Dai, B., Fidler, S., Urtasun, R., & Lin, D. (2017). Towards diverse and natural image descriptions via a conditional gan. In Proceedings of the IEEE International Conference on Computer Vision (pp. 2970-2979).

[57] Odena, A., Olah, C., & Shlens, J. (2017, July). Conditional image synthesis with auxiliary classifier gans. In International conference on machine learning (pp. 2642-2651). PMLR.

[58] Iyer, A., Dey, B., Dasgupta, A., Chen, W., & Chakraborty, A. (2019). A conditional generative model for predicting material microstructures from processing methods. arXiv preprint arXiv:1910.02133.

[59] Banko, L., Lysogorskiy, Y., Grochla, D., Naujoks, D., Drautz, R., & Ludwig, A. (2020). Predicting structure zone diagrams for thin film synthesis by generative machine learning. Communications Materials, 1(1), 1-10.

[60] Agarwala, M., Bourell, D., Beaman, J., Marcus, H., & Barlow, J. (1995). Direct selective laser sintering of metals. Rapid Prototyping Journal.

[61] Goodridge, R. D., Tuck, C. J., & Hague, R. J. M. (2012). Laser sintering of polyamides and other polymers. Progress in Materials science, 57(2), 229-267.

[62] Kruth, J. P., Mercelis, P., Van Vaerenbergh, J., Froyen, L., & Rombouts, M. Binding mechanisms in selective laser sintering and selective laser melting. Rapid prototyping journal. (2005).

[63] Sing, S. L., Yeong, W. Y., Wiria, F. E., Tay, B. Y., Zhao, Z., Zhao, L., ... & Yang, S. Direct selective laser sintering and melting of ceramics: a review. Rapid Prototyping Journal. (2017).

[64] Beyer, H., Ross, W., Rudolph, R., Michaelis, A., Uhlenbusch, J., & Viöl, W. Interaction of CO_2 laser pulses of microsecond duration with Al_2O_3 ceramic substrates. Journal of applied physics, 70(1), 75-81. (1991).

[65] Geng, X., Tang, J., Sheridan, B., Sarkar, S., Tong, J., Xiao, H., ... & Peng, F. (2021). Ultra-Fast Laser Fabrication of Alumina Micro-Sample Array and High-Throughput Characterization of Microstructure and Hardness. Crystals, 11(8), 890.

[66] Schwab, K. The fourth industrial revolution. Currency. (2017).

[67] Vaidya, S., Ambad, P., & Bhosle, S. Industry 4.0–a glimpse. Procedia manufacturing, 20, 233-238. (2018).

[68] Rawat, D. B., Brecher, C., Song, H., & Jeschke, S. Industrial internet of things: Cybermanufacturing systems. Cham, Switzerland: Springer. (2017).

[69] Sisinni, E., Saifullah, A., Han, S., Jennehag, U., & Gidlund, M. Industrial internet of things: Challenges, opportunities, and directions. IEEE Transactions on Industrial Informatics, 14(11), 4724-4734. (2018).

[70] Grasso, M., & Colosimo, B. M. (2017). Process defects and in situ monitoring methods in metal powder bed fusion: a review. Measurement Science and Technology, 28(4), 044005.

[71] Clijsters, S., Craeghs, T., Buls, S., Kempen, K., & Kruth, J. P. (2014). In situ quality control of the selective laser melting process using a high-speed, real-time melt pool monitoring system. The International Journal of Advanced Manufacturing Technology, 75(5-8), 1089-1101.

[72] Zhang, Y., Fuh, J. Y., Ye, D., & Hong, G. S. (2019). In-situ monitoring of laser-based PBF via off-axis vision and image processing approaches. Additive Manufacturing, 25, 263-274.

[73] Arjovsky, M., Chintala, S., & Bottou, L. (2017, July). Wasserstein generative adversarial networks. In International conference on machine learning (pp. 214-223). PMLR.

[74] Karras, T., Aila, T., Laine, S., & Lehtinen, J. (2017). Progressive growing of gans for improved quality, stability, and variation. arXiv preprint arXiv:1710.10196.

[75] Wang, T. C., Liu, M. Y., Zhu, J. Y., Tao, A., Kautz, J., & Catanzaro, B. (2018). High-resolution image synthesis and semantic manipulation with conditional gans. In Proceedings of the IEEE conference on computer vision and pattern recognition (pp. 8798-8807).

[76] LeCun, Y., & Bengio, Y. (1995). Convolutional networks for images, speech, and time series. The handbook of brain theory and neural networks, 3361(10), 1995.

[77] Krizhevsky, A., Sutskever, I., & Hinton, G. E. (2012). Imagenet classification with deep convolutional neural networks. Advances in neural information processing systems, 25, 1097-1105.

[78] Simonyan, K., & Zisserman, A. (2014). Very deep convolutional networks for large-scale image recognition. arXiv preprint arXiv:1409.1556.

[79] Szegedy, C., Liu, W., Jia, Y., Sermanet, P., Reed, S., Anguelov, D., ... & Rabinovich, A. (2015). Going deeper with convolutions. In Proceedings of the IEEE conference on computer vision and pattern recognition (pp. 1-9).

[80] Sedel, L., & Raould, A. (2007). Engineering aspect of alumina on alumina hip prosthesis. Proceedings of the Institution of Mechanical Engineers, Part H: Journal of Engineering in Medicine, 221(1), 21-27.

[81] Ibarra, A., & Hodgson, E. R. (2004). The ITER project: the role of insulators. Nuclear Instruments and Methods in Physics Research Section B: Beam Interactions with Materials and Atoms, 218, 29-35.

[82] Prajzler, V., Salamon, D., & Maca, K. (2018). Pressure-less rapid rate sintering of pre-sintered alumina and zirconia ceramics. Ceramics International, 44(9), 10840-10846.

[83] Huckabee, M. L., ML, H., & PALMOUR, H. I. (1972). Rate controlled sintering of fine-grained Al_2O_3.

[84] Deckers, J., Meyers, S., Kruth, J. P., & Vleugels, J. (2014). Direct selective laser sintering/melting of high density alumina powder layers at elevated temperatures. Physics Procedia, 56, 117-124.

[85] Fayed, E. M., Elmesalamy, A. S., Sobih, M., & Elshaer, Y. (2018). Characterization of direct selective laser sintering of alumina. The International Journal of Advanced Manufacturing Technology, 94(5), 2333-2341.

[86] Wang, J., & Perez, L. (2017). The effectiveness of data augmentation in image classification using deep learning. Convolutional Neural Networks Vis. Recognit, 11.

[87] Mu S, Hong Y, Huang H, Ishii A, Lei J, Song Y, Li Y, Brinkman KS, Peng F, Xiao H, Tong J. A "Novel Laser 3D Printing Method for the Advanced Manufacturing of Protonic Ceramics." *Membranes (Basel)*. **10**(5). (2020).

[88] ASTM Standard C33, 2003a, "Specification for Concrete Aggregates," ASTM International, West Conshohocken, PA, 2003

[89] Abraham, N. B., Lugiato, L. A., & Narducci, L. M. Overview of instabilities in laser systems. JOSA B, 2(1), 7-14. (1985).

[90] Zeng, K. Optimization of support structures for selective laser melting. (2015).